



UNIVERSITÀ DI PARMA

ARCHIVIO DELLA RICERCA

University of Parma Research Repository

Fluid pressure cycles, variations in permeability, and weakening mechanisms along low-angle normal faults: The tellaro detachment, Italy

This is the peer reviewed version of the following article:

Original

Fluid pressure cycles, variations in permeability, and weakening mechanisms along low-angle normal faults: The tellaro detachment, Italy / Clemenzi, Luca; Storti, Fabrizio; Balsamo, Fabrizio; Molli, Giancarlo; Ellam, Rob; Mucchez, Philippe; Swennen, Rudy. - In: GEOLOGICAL SOCIETY OF AMERICA BULLETIN. - ISSN 0016-7606. - 127:11-12(2015), pp. 1689-1710. [10.1130/B31203.1]

Availability:

This version is available at: 11381/2809173 since: 2016-07-25T18:23:41Z

Publisher:

Geological Society of America

Published

DOI:10.1130/B31203.1

Terms of use:

Anyone can freely access the full text of works made available as "Open Access". Works made available

Publisher copyright

note finali coverpage

(Article begins on next page)

1 **[[Supplemental material only cited in Figure 9 –11 captions. Add in-text citation(s) and**
2 **corresponding footnote (superscript 1).]]**

3 *Clemenzi et al.*

4 *Fluid pressure cycles, variations in permeability, and weakening mechanisms, Tellaro*
5 *detachment, Italy*

6 †E-mail address: luca.clemenzi@unipr.it

7 *GSA Bulletin*; Month/Month 2015; v. 1xx; no. X/X; p. 000–000; doi: 10.1130/B31203.1; 15
8 figures; Data Repository item 2015xxx.

9 ¹GSA Data Repository item 2015xxx, **[[Q: please provide a brief description. Q]]**, is available
10 at <http://www.geosociety.org/pubs/ft2015.htm> or by request to editing@geosociety.org.

11

12 **Fluid pressure cycles, variations in permeability, and weakening**
13 **mechanisms along low-angle normal faults: The Tellaro**
14 **detachment, Italy**

15 **Luca Clemenzi^{1,†}, Fabrizio Storti¹, Fabrizio Balsamo¹, Giancarlo Molli^{1,2}, Rob Ellam³,**
16 **Philippe Muechez⁴, and Rudy Swennen⁴**

17 ¹*Natural and Experimental Tectonics Research Group (NEXT), Department of Physics and Earth*
18 *Sciences “Macedonio Melloni,” University of Parma, I-43124 Parma, Italy*

19 ²*Department of Earth Sciences, University of Pisa, Via S. Maria, 53, I-56126 Pisa, Italy*

20 ³*SUERC **[[Please spell out SUERC at first use here.]]**, Rankine Avenue, Scottish Enterprise*
21 *Technology Park, East Kilbride, G75 0QF, Scotland, UK*

22 ⁴*Department of Earth and Environmental Sciences, KU Leuven, Celestijnenlaan 200E, B-3001*

23 *Heverlee, Belgium*

24 **ABSTRACT**

25 Classical frictional fault reactivation models indicate that slip along misoriented fault
26 planes is not possible under most conditions. Nevertheless, active or exhumed low-angle normal
27 faults have been described in many settings worldwide. This discrepancy is addressed by
28 contrasting models: (1) those proposing that low-angle normal faults result from postkinematic
29 passive rotation of former high-angle extensional faults; and (2) those proposing that specific
30 conditions can promote slip along misoriented fault planes. This paper describes the Tellaro
31 detachment, a mid–late Miocene low-angle normal fault that was responsible for ~500 m of
32 tectonic vertical thinning in the carbonate-dominated Triassic to Lower Miocene succession of
33 the Northern Apennines, Italy. By integrating structural, petrographic, isotopic, and fluid
34 inclusion data, we show that: (1) the main kinematic activity of the Tellaro detachment occurred
35 between ~8 and 4 km depths and peak temperature ~190 °C; (2) dilational breccias, tens of cubic
36 meters in volume, are frequently associated with major low-angle fault segments; (3) slip along
37 misoriented planes was favored by elevated fluid pressures and low differential stress; and (4)
38 the fault system was characterized by transient permeability pulses and overpressure buildups,
39 associated with multiple fracturing and cementation events that caused the downward migration
40 of master slip surfaces.

41 Results presented in this study show that: (1) in a fluid-active regime, continental crustal
42 thinning can occur for shallow values of fault dip; (2) low-angle normal faults have a great
43 influence on fluid circulation within the upper crust; and (3) episodic permeability enhancement

44 and destruction in detachment faults can promote overpressure buildups, triggering deformation
45 episodes.

46 INTRODUCTION

47 Understanding whether extensional detachment fault systems can be activated at very
48 shallow dip **or if they** result from the passive postkinematic rotation of former high-angle
49 “Andersonian” fault systems is a matter of long-lasting debate involving field investigation,
50 geochemical and geophysical evidence, and analogue and numerical modeling (Lister et al.,
51 1986; Bradshaw and Zoback, 1988; Yin, 1989; Melosh, 1990; Buck, 1991; Axen, 1992; Scott
52 and Lister, 1992; Lavier et al., 1999; Lavier and Buck, 2002; Smith et al., 2008; Ranero and
53 Pérez-Gussinyé, 2010; Collettini, 2011). Despite intensive studies, a universal solution is not yet
54 available, and the question whether slip can occur along mechanically misoriented slip surfaces,
55 allowing the routine coexistence of low- and high-angle faults, is still open. Indeed, as predicted
56 by frictional slip models, slip along misoriented slip surfaces is not possible in most conditions,
57 and the creation of new, optimally oriented faults should be mechanically favored **given** the
58 coefficient of friction typical for most common rocks (Anderson, 1951; Byerlee, 1978).
59 Nevertheless, slip along misoriented fault planes can be promoted by specific conditions, such as
60 elevated fluid pressure and low differential stress, the presence of low-friction minerals along
61 slip surfaces (e.g., Sibson, 1985), or fault zone weakening associated with diffusive mass transfer
62 processes (e.g., pressure solution creep; Collettini and Holdsworth, 2004; Gratier et al., 2011,
63 2013; Mitterpergher et al., 2011). Accordingly, the structural and hydraulic architecture of fault
64 zones plays a fundamental role to promote, or prevent, the kinematic activity of misoriented
65 faults. In particular, the typical conduit-barrier hydraulic architecture of fault zones in cohesive
66 low-porosity rocks (e.g., Caine et al., 1996; Storti et al., 2003) can have a twofold effect on fluid

67 circulation in the upper crust: (1) fault cores can act as impermeable barriers promoting fluid
68 overpressure (Gudmundsson, 2001; Miller et al., 2004; Collettini et al., 2006a); and (2) damage
69 zones can constitute high-permeability networks allowing fluid circulation, which, under certain
70 circumstances, can promote the formation of low-friction hydrous clay minerals (Hubbert and
71 Rubey, 1959; Davis et al., 1983; Dahlen et al., 1984; Sibson et al., 1988; Dahlen, 1990; Moore
72 and Vrolijk, 1992; Kirschner and Kennedy, 2001; Collettini and Holdsworth, 2004; Fagereng et
73 al., 2010; Lacroix et al., 2013). This can occur both when deep hot fluids migrate upward or
74 when cold surface-derived fluids infiltrate at depth (Wickham and Taylor, 1987; Fricke et al.,
75 1992; Morrison, 1994; Morrison and Anderson, 1998; Bebout et al., 2001; Mulch et al., 2004,
76 2006; Verhaert et al., 2004, 2009; Person et al., 2007; Ingebritsen and Manning, 2010; Rossetti et
77 al., 2011; Gottardi et al., 2011; Gébelin et al., 2011). Fluid circulation along fault zones
78 commonly causes fracture cementation and, possibly, host-rock metasomatism (e.g., Chester and
79 Logan, 1986; Hacker, 1997; Laubach et al., 2010), thus producing significant changes in their
80 rheology and strength.

81 In this paper, we describe the structural architecture and the paleofluid evolution of the
82 Tellaro detachment (Storti, 1995), an exhumed low-angle extensional fault system exposed in the
83 internal (westernmost) portion of the Northern Apennines (Italy), which was active in late
84 Miocene times (Storti, 1995) during the late Cenozoic exhumation of the axial zone of the
85 mountain belt. Our data indicate that the Tellaro detachment was characterized by
86 contemporaneous slip of misoriented low-angle faults and subsidiary high-angle faults in low-
87 strain shear lenses, associated with a complex paleofluid evolution involving multiple episodes
88 of fracturing and cementation events during cyclic variations in permeability. Results presented
89 in this study contribute to support the notions that low-angle fault zones have a great influence

90 on the time-space evolution of fluid circulation within the upper crust, and that fault activity can
91 occur also for shallow values of fault dip, which ensures much higher amounts of crustal
92 thinning, compared to high-angle faulting.

93 **GEOLOGICAL SETTING**

94 The Apenninic segment of the Alpine-Himalayan orogenic system **was** growing in
95 Cenozoic times due to the southwestward subduction, and the associated slab retreat, of the
96 Adria plate below the European plate (Malinverno and Ryan, 1986; Royden, 1988; Dewey et al.,
97 1989; Patacca et al., 1990; Doglioni, 1991). The remnants of the Jurassic Ligurian Ocean and of
98 the thinned passive margin of the Adria plate accreted in the Northern Apennines (Boccaletti et
99 al., 1971; Elter and Pertusati, 1973), resulting in a complex three-dimensional orogenic
100 architecture (Fig. 1A; Elter, 1975). In its internal portion, the thrust wedge includes, from bottom
101 to top: (1) the Apuane and Massa metamorphic thrust nappes, reaching high-pressure (HP)
102 greenschist facies (estimated deepest burial ~20 and 25 km, respectively; Di Pisa et al., 1985;
103 Franceschelli et al., 1986; Molli et al., 2000a, 2000b, 2002); (2) the nonmetamorphic Triassic to
104 Lower Miocene sedimentary succession of the “Tuscan Nappe”; and (3) the nonmetamorphic to
105 very low-metamorphic-grade Jurassic–Cretaceous Subligurian and Ligurian ophiolite-bearing
106 units and the middle Eocene to Pliocene Epiligurian wedge-top sediments (Elter, 1975; Molli,
107 2008). The first-order nappe pile underwent significant synorogenic tectonic thinning by low-
108 angle extensional faulting (Carmignani and Kligfield, 1990; Carmignani et al., 1994; Storti,
109 1995; Decandia et al., 1998; Brogi, 2004; Molli, 2008; Carlini et al., 2013; Clemenzi et al.,
110 2014), **which was** then overprinted by out-of-sequence thrusting (Argnani, 2002; Boccaletti et
111 al., 2011; Bonini et al., 2013; Clemenzi et al., 2014) and by further extensional deformations that
112 also triggered Upper Miocene to Pleistocene magmatic activity in the central and southern

113 sectors of the belt (e.g., Elter, 1975; Carmignani et al., 1995; Storti, 1995; Barchi et al., 1998;
114 Jolivet et al., 1998; Brogi and Liotta, 2006; Collettini et al., 2006b; Brogi, 2008; Rossetti et al.,
115 2008). The deformation conditions of the Tuscan succession within the Apenninic thrust wedge
116 have been constrained by means of different methodologies, including vitrinite reflectance
117 (Reutter et al., 1983), stable isotopes (Carter and Dworkin, 1990), fission-track analysis on
118 apatite (Abbate et al., 1994; Zattin et al., 2002; Balestrieri et al., 2003) and zircon (Bernet et al.,
119 2004; Fellin et al., 2007), fluid inclusion microthermometry (Montomoli et al., 2001; Montomoli,
120 2002), illite crystallinity (Cerrina Feroni et al., 1983; Carosi et al., 2003), calcite-dolomite
121 geothermometry (Carosi et al., 2003), and **transmission electron microscopy (TEM)**
122 microstructure analysis (Molli et al., 2011). The maximum tectonic burial of the Tuscan
123 succession, related to the first thrusting event, took place ca. 20 Ma (Fellin et al., 2007, and
124 references therein), with the deepest conditions at ~7–8 km depth and 200–250 °C (Molli et al.,
125 2011). The nominal geothermal gradients, corresponding to the different paleotemperatures
126 calculated by the different authors, ranges between 18 and 41 °C/km (Molli et al., 2011, and
127 references therein) but recent Raman spectroscopy of carbonaceous material (RSCM) indicated
128 that the lowermost values are the more appropriate for the area investigated in this paper (Molli,
129 2014, personal commun.).

130 The Punta Bianca promontory, in the innermost part of the Northern Apennines, exposes
131 the complete stack of the nappe pile (Fig. 1B), folded in a northwestward-plunging anticline
132 (Fig. 1C). Deformation in this area is polyphase and includes: (1) the NE-vergent stacking of
133 first-order tectonostratigraphic units during the early–middle Miocene; (2) middle to late
134 Miocene out-of-sequence thrusting, with the involvement of previously juxtaposed units in
135 antiformal stack and duplex structures, and related gravity-driven tectonic thinning of the

136 overlying portion of the wedge, mainly by low-angle normal faulting; and (3) Late Miocene?–
137 Pliocene to Quaternary crustal extension associated with the eastward migration of both the
138 contractional deformation front and the Tyrrhenian back-arc eastern shoulder (Elter et al., 1975).
139 The Tellaro detachment, investigated in detail in this paper, is the best exposed among the late-
140 orogenic low-angle extensional fault systems and is characterized by spectacular outcrops along
141 the shoreline between the villages of Lerici and Tellaro (Fig. 2). This fault system mainly affects
142 and dismembers the kilometer-thick Tuscan basinal succession, composed of Triassic to Lower
143 Cretaceous carbonates, Lower Cretaceous to Upper Oligocene shales, and Upper Oligocene to
144 Lower Miocene flysch sandstones (Fig. 1D). The Tellaro detachment is dissected by high-angle,
145 NW-SE–striking Pliocene–Pleistocene fault zones (Fig. 1C; Storti, 1995).

146 **METHODS**

147 Detailed mapping and structural analysis were carried out in the study area to (1) unravel
148 the three-dimensional architecture of the low-angle extensional fault system, (2) characterize the
149 associated damage zone, and (3) determine the tectonic transport direction. The latter was
150 calculated in each field site by using the attitude of S-C fabrics, fault slickenlines and
151 corrugations, and fault-related veins (Passchier and Trouw, 2005). Structural data are reported
152 using the right-hand rule (strike/dip), and stereographic projections were plotted on lower-
153 hemisphere diagrams using the Daisy3 software (Salvini, 2014).

154 To characterize the structural association of fault rocks and the type of fluids involved in
155 the deformation, 42 oriented samples were collected along the exposed fault zones. For
156 comparison purposes, additional sampling was carried out (1) in one location along the Pitelli
157 detachment (Storti, 1995), another low-angle extensional fault zone geometrically overlying the
158 Tellaro detachment, (2) in one outcrop at the southern termination of the Punta Bianca

159 promontory, where a subsidiary low-angle shear zone cuts through the Triassic metamorphic
160 rocks, and (3) in two locations in relatively undeformed areas, several hundreds of meters away
161 from major fault zones. In all cases, sampled rocks are Tuscan carbonates similar to those
162 affected by the Tellaro detachment, and sampling locations were selected based on good
163 exposure conditions, which allowed appropriate control over the presence/absence of relevant
164 nearby fault zones. In text and figures, samples are named with the PB label followed by a
165 progressive two-digit number. Since many vein generations are generally present in each sample
166 and show remarkably different features, a suffix is added to refer to each vein (e.g., PB22-1,
167 PB22-2). Each sample was cut to obtain two “mirrored” slabs, one of which was polished and
168 stained with Alizarin red and potassium ferricyanide to easily discriminate different carbonate
169 minerals such as calcite, dolomite, and their respective iron-rich equivalents. From the other slab,
170 thin sections and wafers for microthermometry were prepared. Microstructural and petrographic
171 analyses of 43 thin sections were carried out using optical and cold cathodoluminescence (CL)
172 microscopy. The latter was performed with a Techosyn 8200 Mark II cold CL stage operated at
173 12 kV and 200 μ A **gun** current.

174 Isotopic analyses were performed on microsamples of veins and host rocks.
175 Microsamples were drilled from the stained slabs (after removal of the material altered by
176 staining) with a dental drill. For stable oxygen and carbon isotope analysis, carbonate powders
177 were reacted with 100% phosphoric acid at 70 °C using a Gasbench II connected to a Thermo
178 Finnigan Delta V+ mass spectrometer. All values are measured in per mil (‰) relative to the
179 Vienna Peedee belemnite (**VPDB**) standard. For convenience purposes, oxygen values were also
180 converted **into Vienna standard mean ocean water** (SMOW) notation with the formula

181
$$\delta^{18}O_{SMOW} = 1.03086 \cdot \delta^{18}O_{V-PDB} + 30.86 \text{ (1)}$$

182 (Friedman and O'Neil, 1977). Reproducibility was checked by replicate analysis of selected
183 samples and laboratory standards and is better than $\pm 0.07\text{‰}$ and $\pm 0.09\text{‰}$ for oxygen and carbon
184 isotope compositions, respectively. Isotope fractionation curves for calcite precipitation were
185 computed with the formula

186
$$10^3 \cdot \ln \alpha = \frac{A \cdot 10^6}{T^2} + B \quad (2)$$

187 using $A = 2.78$ and $B = -2.89$ (Friedman and O'Neil, 1977). For radiogenic strontium analyses,
188 carbonate powders were leached in 1 *M* ammonium acetate and digested in 2.5 *M* HCl. Sr was
189 separated by conventional cation exchange chromatography, and total procedure blanks were less
190 than 100 pg. The $^{87}\text{Sr}/^{86}\text{Sr}$ ratio was measured on a VG Sector 54–30 mass spectrometer operated
191 in dynamic mode. Mass fractionation was corrected assuming $^{86}\text{Sr}/^{88}\text{Sr} = 0.1194$ using an
192 exponential law. NIST SRM987 gave 0.710249 ± 16 (2 SD, $n = 17$).

193 Fluid inclusions were analyzed in doubly polished thick sections (wafers), which were
194 mapped with a standard petrographic microscope. The wafers were subsequently broken into
195 smaller pieces (chips) and analyzed in a Linkam THMSG600 heating-cooling stage, calibrated
196 weekly with SynFlinc synthetic standards. Whenever possible, the fluid inclusion assemblage
197 (FIA) approach was followed (Goldstein and Reynolds, 1994). FIAs are composed of a few
198 inclusions (generally 5–10) that do not show any relationship to fractures, occur randomly in the
199 sample, and are considered to be representative of the same trapping event associated with
200 trapping or recrystallization conditions of the analyzed mineral. A few isolated inclusions were
201 measured as well, but only if many of them were found in the same vein. Samples with only a
202 few isolated inclusions (less than 5 per vein) were not further considered. In order to avoid any
203 artificial stretching of the inclusions, heating was always performed before freezing, and each
204 chip was heated only once. Individual chips were then examined through CL microscopy to

205 exclude recrystallization of the crystals hosting the measured inclusions. Analyzed inclusions
206 were 2–5 μm in size and monophasic (liquid) or two-phase (aqueous liquid + vapor bubble) at
207 room temperature. Vapor bubble size ranged from 10% to 20% in volume in analyzed two-phase
208 inclusions; inclusions with bigger bubbles were rare and were not further considered. Three
209 temperatures were routinely measured in two-phase inclusions: homogenization to the liquid
210 phase (T_h), indicative of the minimum trapping temperature of the inclusion; first melting
211 temperature (T_{fm}), associated with the fluid composition; and final ice melting ($T_{m\ ice}$), which is
212 inversely proportional to the salt content of the aqueous phase. Fluid salinity was computed from
213 measured T_m values using the software FLUIDS (Bakker, 2003). Pressure correction was applied
214 to the T_h values to determine the actual trapping conditions (temperature and pressure) of each
215 FIA. The trapping conditions were defined by the intersection of the fluid pressure-temperature
216 gradient (computed from the estimated geothermal gradient) and the appropriate isochore
217 (computed from the salinity and T_h of each group of inclusions). This methodology is affected by
218 the selection of specific geothermal and fluid pressure gradients at depth. For the geothermal
219 gradient, a value of 20 $^{\circ}\text{C}/\text{km}$ is considered the most appropriate for the area of interest (see
220 section 2 **[[Section numbers not used herein. Cite section title instead.]]**). For the fluid
221 pressure gradient, both hydrostatic and lithostatic conditions were used. Monophasic inclusions
222 were cooled to $-20\ ^{\circ}\text{C}$ for 2 wk in order to check their possible metastability. If they were still
223 monophasic after this treatment, a vapor bubble was artificially created via rapid heating-freezing
224 cycles, and then T_{fm} and $T_{m\ ice}$ temperatures were measured in standard freezing experiments.
225 Some inclusions showed a metastable behavior during reheating after being frozen: Their bubble
226 returned to the original prefreezing size at temperatures above $0\ ^{\circ}\text{C}$ despite the slow heating rate
227 ($0.1\ ^{\circ}\text{C}/\text{min}$).

228 **STRUCTURAL ARCHITECTURE**

229 The Tellaro detachment is ~30–50 m thick and includes major low-angle (detachment)
230 and subsidiary high-angle extensional faults well exposed in low-strain shear lenses. The master
231 detachment is located at the base of the Cretaceous shales of the Scaglia Toscana Formation (Fig.
232 2), but it is usually not well exposed due to vegetation, soil cover, and anthropization. In the
233 footwall damage zone of this master detachment, other low-angle fault zones, with variable
234 extensional offset, affect the Triassic to Jurassic Formations of the Tuscan succession. The latter
235 **are** very well exposed along the Tyrrhenian shoreline (Figs. 3 and 4). In its northernmost portion,
236 near Lerici, a low-angle fault segment with minor offset also crosscuts the folded basal tectonic
237 contact between nonmetamorphic upper Triassic limestones and the underlying mid-Triassic
238 metamorphic clastic rocks (Fig. 2). The tectonic transport direction of the fault system,
239 determined in 14 field sites, is top-to-the-NE, with local values ranging from N010E to N080E
240 (Fig. 2). The degree of tectonic thinning is quite variable along strike, reaching its maximum
241 near Lerici village, where ~500 m of thinning is associated with the complete elision of the
242 Jurassic Formations and the direct juxtaposition of the Upper Cretaceous shales of the Scaglia
243 Toscana Formation on the Upper Triassic limestones of the La Spezia Formation. The degree of
244 tectonic thinning slightly decreases to the southeast, where the Jurassic formations are preserved
245 as meter- to decameter-scale lenses bounded by anastomosing low-angle and high-angle faults
246 (Figs. 3A–3D). The cumulative offset of the Tellaro detachment fault system can be roughly
247 estimated to be ~1.3 km based on the assumption of a 25° average fault dip (see section
248 7.2[[**Section numbers not used herein. Cite section title instead.**]]) and the stratigraphic
249 separation.

250 Low-angle master slip surfaces are generally organized in juxtaposed segments with
251 similar attitude, and with spacing ranging from ~1 m to tens of meters (Fig. 5). Fault zones are
252 commonly marked by S-C arrays of tectonic stylolites (Fig. 4). Slip surfaces are typically
253 decorated by slickenlines and are characterized by centimeter- to meter-scale corrugations
254 oriented parallel to the tectonic transport direction (Fig. 3E). In the proximity of the biggest
255 corrugations, meter-scale tight folds with corrugation-parallel axes are present in the hanging-
256 wall damage zones (Fig. 3F). The close correlation between hanging-wall folds and major fault
257 corrugations suggests a genetic connection between these two deformation features. The attitude
258 of low-angle fault zones is clustered around a NW-SE strike and a shallow NE dip (N320/10;
259 Fig. 2B). Most subsidiary faults strike near perpendicular to the local tectonic transport
260 directions, and few ones are near parallel to it (Fig. 2B). NE-dipping synthetic faults are by far
261 the most abundant among the subsidiary faults; they have extensional kinematics and moderate
262 dip values. SW-dipping antithetic subsidiary faults have extensional kinematics and steeper dip
263 values. Subsidiary tear faults, striking parallel to the tectonic transport direction, have strike-slip
264 kinematics and moderate dip values (Fig. 2B). Approaching the master low-angle extensional
265 surfaces, subsidiary faults gradually shallow their dip and eventually sole down into the
266 detachment (Figs. 4 and 5). Slickenlines from both low- and high-angle faults provide the same
267 tectonic transport direction (Fig. 3C).

268 **FAULT ROCK TEXTURE**

269 The Tellaro detachment is characterized by abundant veins, stylolites of tectonic origin
270 (i.e., not due to burial), and localized bodies of dolomitic breccias (Fig. 4).

271 **Stylolites**

272 Tectonic stylolites have subhorizontal to slightly SW-dipping attitude, and are
273 particularly abundant in the footwall of major low-angle fault segments (Fig. 6A). Frequently,
274 dissolution seams are found in S-C arrays with shear planes oriented nearly parallel to the main
275 detachment, and the dissolution seams are oriented at low angle and gently deformed (Fig. 6A).
276 Abundant calcite veins affect stylolite-band lithons and are typically oriented at high angle to
277 them. Synthetic shear cutting through the S-C arrays occurs frequently (Fig. 6B). The orientation
278 of the S-C arrays is indicative of top-to-the-NE tectonic transport directions, consistent with the
279 kinematics obtained from slickensides and corrugations on major fault planes.

280 **Veins**

281 Subvertical syntectonic veins are very abundant in the whole area along the Tellaro
282 detachment, particularly in the footwall damage zones of major low-angle fault segments. Veins
283 are usually filled by calcite, but some veins with dolomite infillings are also present in dolomitic
284 host rocks. Veins have variable orientations (Figs. 2 and 5) and are frequently organized in three
285 sets crosscutting at acute angles (Fig. 6C) and striking parallel to the local tectonic transport
286 direction, orthogonal to it, and at intermediate orientation, respectively. The crosscutting
287 relationships between the three sets are not systematic. In the proximity of low-angle slip
288 surfaces, calcite-filled veins can be much shorter and closely spaced, with irregular, randomly
289 oriented, curved geometry (Figs. 6B and 6D).

290 Dolomite veins generally have a NW-SE orientation, millimeter- to centimeter-scale
291 aperture, and granular equant texture with rhombohedral crystals showing sweeping extinction in
292 crossed-polar microscopy. Crystal size is variable: In smaller veins, crystals range from a few
293 tens up to 200 μm (Fig. 7A). Rare veins with fibrous texture also exist and are crosscut by
294 younger equant granular veins. Sometimes, protobreccias are observed at the margin of veins

295 (Fig. 7B). They extend over a few cubic centimeter rock volumes and are characterized by
296 millimeter-scale clasts with tight-packed fitted-fabric or dilated texture. In the latter case, clasts
297 are partly rotated and separated by millimeter-scale extension veins filled by dolomite cement
298 (crystal size ~100 μm). Occasionally, calcite reopenings are present at the boundary between
299 dolomite veins and dolomitic host (Fig. 7C). Under CL light, dolomite crystals show large cores
300 with dull purple homogeneous luminescence and thin bright purple/red rims at the margins (Fig.
301 7D).

302 Calcite veins occur in any host rock (limestone, dolostones, and dolomitic breccias).
303 Petrographic analysis indicates the presence of multiple generations of infillings, which can be
304 grouped in two first-order types, named “type 1” and “type 2.” Type 1 veins have variable
305 aperture (from a few tens of micrometers up to 2 cm) and are characterized by intense type I
306 twinning indicative of low-temperature deformation (Burkhard, 1993). Type 1 vein texture is
307 granular equant, with larger inequant grains sometimes present toward the middle sector (Fig.
308 7E). Occasionally, parallel comb texture is observed in larger veins, with crystals having an
309 aspect ratio from 5 to 10 (Fig. 7F). Fibrous veins and crack-seal microstructures are rare.
310 Sometimes, thick veins (aperture > 5 mm) are characterized by multiple reopenings, each one
311 with millimeter-scale aperture, highlighted by calcite infillings with different textures or
312 luminescence colors (Figs. 7G and 7H). CL petrography highlights the presence of different
313 calcite generations in type 1 veins, characterized by a **nonluminescence to** dull-brown or bright-
314 orange luminescence and different crosscutting relationships (Fig. 7I). Systematic investigations
315 in more than 30 oriented thin sections, including many differently oriented veins, indicate that
316 the different calcite generations do not have any association with specific vein orientation. Apart
317 from the reopening events, CL shows homogeneous colors at the scale of a single vein among

318 the analyzed samples. Only one type 1 vein was characterized by crystals with growth-zonation
319 luminescence (Fig. 7J).

320 Type 2 veins are smaller (aperture < 0.5 mm) and have a granular equant texture
321 characterized by clean calcite crystals without twinning (Figs. 7C and 7G). Under CL, type 2
322 calcite is characterized by four different luminescence patterns, including: (1) dull brown, (2)
323 dominantly nonluminescent zones with tiny luminescent concentric subzones within the single
324 crystals, (3) bright-yellow luminescent zones, and (4) dull luminescent zones with subzones of
325 various luminescence colors. These different luminescence patterns may coexist within a single
326 vein and are generally associated with progressive infilling (Fig. 7H). Type 2 veins always
327 crosscut or reopen dolomite and type 1 calcite veins.

328 **Dolomitic Breccias**

329 Locally, dolomitic breccia bodies with tabular shape (1–2 m in height and several meters
330 to tens of meter in length) are associated with the low-angle fault zones. The host rock
331 surrounding the dolomitic breccias can be either limestone or dolostones (Figs. 4 and 5).

332 Boundaries between breccias and host rock are irregular and discordant with respect to bedding
333 in the host formations. The bottom boundary is provided by low-angle fault surfaces with large
334 stratigraphic offset, associated with thin (centimeter-scale) dolomite cataclastic bands. With the
335 exception of basal cataclastic bands, texture is homogeneous within the meter-scale brecciated
336 bodies, without remarkable variations between the central and marginal portions. Dolomitic
337 breccias are cut through by the high-angle synthetic subsidiary faults, by widely spaced
338 subvertical calcite veins, and by subhorizontal tectonic stylolites.

339 Dolomitic breccias are characterized by angular clast and cement, while any fine-grained
340 matrix is absent (Figs. 8A and 8B). Texture is not characterized by strong fabrics or preferred

341 orientation of the clasts, and it is very variable, including zones of very high clast/cement ratio
342 and fitted-fabric texture, and zones with lower clast/cement ratio. The different textures coexist
343 close to one another, even at the scale of a single thin section (Fig. 8B), and can be classified as
344 “crackle,” “mosaic,” or “chaotic breccia,” according to Woodcock and Mort (2008). In areas
345 with crackle breccia texture, clasts size ranges from 5 mm to 2 cm; in areas with chaotic breccia
346 texture, clast size ranges from 0.5 to 5 mm, with the majority of them being >2 mm. In both
347 cases, the clast are angular, with sharp borders (Fig. 8C), and are completely recrystallized. They
348 are made of fine-crystalline (50–200 μm size) rhombohedral dolomite crystals (Fig. 8D). The
349 cement between the clasts is microcrystalline dolomite (crystal size < 100 μm) and characterized
350 by a granular equant texture (Fig. 8D). Calcite veins cut the breccias with straight boundaries and
351 show no evidence of recrystallization or calcite infiltration into the breccia (Figs. 8E and 8F). In
352 the bulk of the breccia bodies, there is limited evidence for persistent refracture and reseal during
353 brecciation, and cement does not show fibrous or crack-seal texture, indicating precipitation into
354 voids. Rebrecciation, cemented by ferroan calcite, is only sporadically observed (Fig. 8A).

355 Cataclastic bands associated with fault surfaces at the base of the breccia bodies have a
356 completely different texture (Fig. 8G). Grain-size distributions are more variable, ranging from
357 millimeter-scale clast to fine-grained matrix, and gradually decrease approaching the main slip
358 surfaces. The boundaries between these centimeter-thick cataclastic bands and the crackle to
359 chaotic breccias characterizing the bulk of the breccia bodies are well marked (Fig. 8G).

360 **CEMENT GEOCHEMISTRY AND FLUID INCLUSION DATA**

361 **Stable Oxygen and Carbon Isotopes**

362 Stable isotope analysis was carried out on dolomitic breccia (clasts and cement), dolomite
363 veins, calcite veins, and host rocks. The cumulative plot of all samples (Fig. 9A) shows that host

364 rock values from all the sampling sites cluster together ($+0.5\text{‰} < \delta^{13}\text{C} < +3.5\text{‰}$, $+24\text{‰} < \delta^{18}\text{O} <$
365 $+28\text{‰}$ VSMOW). Such values are partly in agreement with values reported by other authors for
366 Tuscan succession host rocks from other localities. Only two host-rock samples differ from this
367 cluster and have depleted (negative) carbon isotope values. Vein and breccia samples have
368 carbon isotopes generally within the range of the host rocks, with only a few samples showing
369 remarkably depleted values down to -8‰ VPDB. Vein and host-rock samples with depleted
370 carbon isotope are all aligned on the same trend with an oxygen isotope value of $\sim+26\text{‰}$
371 VSMOW. Oxygen isotope values for veins and breccias are characterized by a marked
372 variability over a range that is much wider than that of host rocks ($+15\text{‰} < \delta^{18}\text{O} < +29\text{‰}$
373 VSMOW). Comparing different structural positions, samples from the Tellaro detachment show
374 the greatest oxygen isotope variability, including both the most and the least depleted values.
375 Samples collected far away from major fault zones still show some oxygen isotope variability
376 ($+20\text{‰} < \delta^{18}\text{O} < +26\text{‰}$ VSMOW). The only samples showing almost no oxygen isotope
377 variability are those from the Pitelli detachment ($+23\text{‰} < \delta^{18}\text{O} < +25\text{‰}$ VSMOW). The latter,
378 however, are by far less numerous.

379 Along the Tellaro detachment (Fig. 9B), a small difference exists between calcite and
380 dolomite hosts, with the latter having slightly more depleted oxygen and enriched carbon isotope
381 values. Dolomitic breccias show clustered carbon and variable oxygen isotopic compositions
382 ($+3\text{‰} < \delta^{13}\text{C} < +4\text{‰}$, $+23\text{‰} < \delta^{18}\text{O} < +29\text{‰}$ VSMOW). Dolomite veins show slightly variable
383 carbon and clustered oxygen isotopic compositions ($+0.5\text{‰} < \delta^{13}\text{C} < +3\text{‰}$, $\delta^{18}\text{O} \approx +27\text{‰}$
384 VSMOW). Calcite vein isotope values are aligned along two trends, one trend with carbon
385 isotope values in the range of the host rock and broadly variable oxygen isotope values ($+15\text{‰} <$
386 $\delta^{18}\text{O} < +26\text{‰}$ VSMOW), and the other trend with depleted carbon and less variable oxygen

387 isotope values ($-7\text{‰} < \delta^{13}\text{C} < +1\text{‰}$, $+23\text{‰} < \delta^{18}\text{O} < +27\text{‰}$ VSMOW). Such variability in
388 calcite veins shows no correlation with vein orientation or the stratigraphic formations and only a
389 partial correlation with the first-order subdivision in successive calcite infill generations (type 1
390 or 2; Fig. 9B). Indeed, veins with depleted carbon ($-7\text{‰} < \delta^{13}\text{C} < +1\text{‰}$) are preferentially type 2,
391 but veins with more enriched carbon and broadly variable oxygen isotope can be either type 1 or
392 type 2.

393 **Fluid Inclusion Microthermometry**

394 Twenty-five doubly polished wafers of Tellaro detachment samples were used to analyze
395 fluid inclusions in dolomite and type 1 and type 2 calcite veins. Dolomite crystals in dolomite
396 veins can have either a cloudy or clean aspect, characterized by more or less abundant fluid
397 inclusions (Figs. 10A and 10B). Inclusions can occur (1) aligned along planes parallel to the
398 crystal margins and different growth sectors, (2) as planes of pseudosecondary inclusions, or (3)
399 as isolated spots inside the crystals. Many inclusions are rectangular or prismatic, but shapes that
400 are more irregular are also present. They are variable in size, from $\sim 2\ \mu\text{m}$ to $5\ \mu\text{m}$, and biphase
401 liquid + vapor at room temperature, with the vapor bubble being 10%–20% in volume.
402 Microthermometric analysis was carried out on 15 inclusions of primary origin, 2–5 μm in size,
403 organized in four FIAs, selected from two different dolomite veins. Homogenization
404 temperatures (T_h) showed consistent results, clustered at $150\ \text{°C}$ (Fig. 10G). First melting
405 temperatures (T_{fm}) ranged between $-25\ \text{°C}$ and $-20\ \text{°C}$, but they could be measured only in a few
406 inclusions; they were interpreted to indicate a dominantly H_2O -NaCl fluid system. Final ice
407 melting temperatures ($T_{m\text{ice}}$) were slightly variable (Fig. 10H), with median value at $-15.7\ \text{°C}$,
408 corresponding to 19.2% wt. eq. NaCl (Bodnar, 1993).

409 Type 1 calcite, due to the intracrystalline deformation and abundant twinning, is mainly
410 characterized by secondary inclusion trails aligned along twinning planes, and by isolated
411 inclusions of primary or unknown origin, randomly distributed in the space between twinning
412 planes (Figs. 10C and 10D). Microthermometric analysis was carried out on the latter, while
413 secondary inclusion trails were not further considered. Isolated inclusions were often too small
414 ($<1\ \mu\text{m}$) for successful phase change observations, so only samples containing sufficiently large
415 inclusions (2–5 μm) were selected. Moreover, due to the intense deformation that affected calcite
416 crystals in type 1 veins, the possible effects of fluid inclusion stretching and leakage had to be
417 evaluated by comparison of data measured in multiple inclusions within the same assemblage.
418 For this reason, veins containing only few (less than 5) isolated inclusions were rejected. Thirty-
419 four veins were analyzed after careful petrography and fluid inclusion selection. Based on these
420 criteria, reliable microthermometry data were obtained from only four veins. The analyzed
421 inclusions were regularly shaped, 2–5 μm in size, and biphasic liquid + vapor at room
422 temperature, with the vapor bubble being 10%–20% in volume. Rare inclusions with larger
423 vapor bubbles, up to 60% in volume, were present but not analyzed. Homogenization (T_h), first
424 melting (T_{fm}), and final melting ($T_{m\ ice}$) temperatures were measured. First ice melting
425 temperatures (T_{fm}) could not be measured in all the inclusions; when available, they ranged
426 between $-25\ ^\circ\text{C}$ and $-13\ ^\circ\text{C}$ and were interpreted to indicate a H_2O -NaCl fluid system.
427 Homogenization (T_h) and final ice melting ($T_{m\ ice}$) temperatures showed remarkable variability.
428 In vein PB21–2, 14 fluid inclusions were measured in four different FIAs. In all assemblages,
429 inclusions showed T_h clustered at $140\ ^\circ\text{C}$ (Fig. 10G) and relatively clustered $T_{m\ ice}$ with a $-1.9\ ^\circ\text{C}$
430 median value (Fig. 10H), corresponding to 3.2% wt. eq. NaCl (Bodnar, 1993). A single fluid
431 inclusion with a much lower $T_{m\ ice}$ of $-14.7\ ^\circ\text{C}$ was also present (Fig. 10H), and it was located

432 within a FIA in which other inclusions showed the more usual ~ -2 °C $T_{m\ ice}$. In vein PB22–2,
433 eight inclusions were measured in two FIAs. In both assemblages, inclusions showed widespread
434 T_h data between 100 °C and 160 °C (Fig. 10G). Careful analysis, however, indicates that most of
435 the measurements (5) cluster within a small range (93–108 °C), while a few measurements (3)
436 are remarkably higher and broadly variable (125–159 °C); the latter are located in both FIAs.
437 Reliable $T_{m\ ice}$ data could be measured in two inclusions, each located in a different FIA, and
438 gave values of -10.5 °C and -1.7 °C (Fig. 10H), corresponding to salinities of 14.4% and 2.9%
439 wt. eq. NaCl (Bodnar, 1993). In vein PB22–3, seven inclusions were measured in two FIAs,
440 showing clustered T_h and $T_{m\ ice}$ values (Figs. 10G and 10H), with 120 °C and -9.5 °C as the most
441 representative and median values, respectively. The latter value corresponds to 13.4% wt. eq.
442 NaCl (Bodnar, 1993). In vein PB17–1, seven inclusions from three FIAs were measured,
443 showing widespread T_h data between 80 °C and 190 °C (Fig. 10G) and clustered $T_{m\ ice}$ data (Fig.
444 10H), with a median value at -14.8 °C, corresponding to 18.5% wt. eq. NaCl (Bodnar, 1993).
445 Careful analysis of the T_h values showed that most of the measurements (6) are within a
446 relatively small range (between 80 °C and 110 °C), while only one inclusion has a remarkably
447 higher temperature (190 °C).

448 Type 2 calcite has a clear aspect, with isolated inclusions of primary or unknown origin.
449 Inclusions are generally small sized (<1 μm), but some bigger inclusions (2–5 μm), monophasic
450 at room temperature, were found (Figs. 10E and 10F). Such inclusions are of the same size as
451 biphasic inclusions of type 1 calcite and were still monophasic after 2 wk at -20 °C; they
452 nucleated a bubble only after multiple rapid heating-freezing cycles. This process resulted in
453 biphasic liquid + vapor inclusions on which standard freezing experiments could be performed.
454 Phase changes associated with the first ice melting could not be observed in any sample. Final

455 ice melting temperatures ($T_{m\text{ ice}}$) were measured and showed clustered results with a $-0.4\text{ }^{\circ}\text{C}$
456 median value (Fig. 10I), corresponding to 0.7% wt. eq. NaCl (Bodnar, 1993).

457 **Radiogenic Strontium Isotopes**

458 Strontium isotope ratios were analyzed from eight type 1 calcite veins, which were
459 selected based on the availability of microthermometric data and their stable isotope signature
460 (e.g., those with the most depleted or most enriched oxygen isotope values). For comparison
461 purposes, the $^{87}\text{Sr}/^{86}\text{Sr}$ of analyzed samples was compared with seawater composition at the time
462 of Tellaro detachment fault activity (late Miocene) and with the expected composition for
463 carbonates of the same age as the Tuscan succession (Upper Triassic to Upper Cretaceous;
464 McArthur et al., 2001). The $^{87}\text{Sr}/^{86}\text{Sr}$ values in the analyzed veins cluster around three different
465 values and show a partial correlation with the stable isotope signature (Fig. 11). A first cluster
466 included four veins showing depleted oxygen ($+21\text{‰} < \delta^{18}\text{O} < +26\text{‰}$ VSMOW) and $^{87}\text{Sr}/^{86}\text{Sr}$
467 values around 0.7080, which is slightly higher than expected values for Upper Triassic to Upper
468 Cretaceous carbonates (e.g., McArthur et al., 2001); fluid inclusion microthermometry data are
469 available for three of those veins and show quite variable homogenization temperatures (110–
470 160 $^{\circ}\text{C}$). The second cluster included three veins showing very depleted oxygen isotope ($+17\text{‰}$
471 $< \delta^{18}\text{O} < +22\text{‰}$ VSMOW) and $^{87}\text{Sr}/^{86}\text{Sr}$ around 0.7085, an intermediate value between late
472 Miocene seawater and expected values for Upper Triassic to Upper Cretaceous carbonates; fluid
473 inclusion microthermometry data were not available for these veins. Finally, only one vein
474 showed depleted oxygen isotope values ($+24\text{‰} < \delta^{18}\text{O} < +27\text{‰}$ VSMOW) and $^{87}\text{Sr}/^{86}\text{Sr}$ values
475 around 0.70915, slightly higher than the values of late Miocene seawater; the homogenization
476 temperatures of the fluid inclusions in this vein are around 90 $^{\circ}\text{C}$.

477 **DISCUSSION**

478 **Stages of Carbonate Precipitation**

479 The Tellaro detachment was associated with a complex paleofluid evolution that involved
480 precipitation of different generations of mineral infillings over a wide range of temperature and
481 depth conditions. Combined microstructural, petrographic, microthermometric, and stable and
482 radiogenic isotope analyses allow us to identify three different main stages within the carbonate
483 precipitation history. The first stage is characterized by the formation of dolomite veins, in which
484 clustered microthermometric and stable isotope data indicate that veins formed either from a
485 fluid of local origin (e.g., a formation fluid buffered by the host rock), or from an external fluid
486 that was rock-buffered due to fluid-rock interactions prior to vein precipitation (Gray et al., 1991;
487 Muchez et al., 1995). Trapping conditions for dolomite veins can be estimated to ~190 °C and
488 8.5 km depth, constrained by the specific isochore (veins PB04–1 and PB05–1) and the
489 assumption that veins formed at an average geothermal gradient of 20 °C/km and hydrostatic
490 fluid pressure conditions during carbonate precipitation (Fig. 12A). The assumption of lithostatic
491 fluid pressure and 20 °C/km geothermal gradient gives unrealistic trapping conditions, i.e.,
492 deeper than the maximum burial experienced by the Tuscan succession in the study area.
493 Intermediate fluid pressure conditions, however, cannot be ruled out.

494 The second stage is associated with the formation of type 1 calcite veins. Available
495 microthermometric data show a remarkable variability in this stage, but individual data from
496 each vein cluster within reasonably small T_h ranges (~20 °C), with the exception of a few outliers
497 likely due to leaking or stretching. Therefore, the variable T_h values are interpreted to reflect the
498 precipitation of each vein infilling at a different temperature. Such observation can imply that
499 either (1) each vein formed at a different depth, and precipitation temperature was controlled by
500 a regional geothermal gradient, or, alternatively, (2) all veins formed nearly at the same depth,

501 and calcite precipitation temperature was controlled by the ambient fluid temperature, which
502 might have been hotter or colder than that of the immediate host rock due to upward or
503 downward migration of the fluids, respectively. The first hypothesis is favored by several
504 observations, including (Fig. 10H): (1) lack of a systematic relationship between homogenization
505 temperatures and fluid salinity, despite the presence of both high-salinity and low-salinity fluids
506 in the different veins; and (2) similar homogenization temperature of inclusions with very
507 different salinities within a single vein. Accordingly, different trapping conditions have been
508 estimated for the analyzed type 1 calcite veins, assuming a constant geothermal gradient and
509 using the specific isochore computed from the most common T_h values (veins PB21–1, PB322–
510 3, and PB22–2), or the minimum measured value in one vein where a clear maximum was not
511 recognizable in the T_h distribution (vein PB17–1). With the assumption of a 20 °C/km
512 geothermal gradient and hydrostatic fluid pressure, estimated trapping conditions for the
513 different veins range from ~180 °C to 95 °C and from ~8 to 4 km depth (Fig. 12A). Also in this
514 case, the assumption of lithostatic fluid pressure and a 20 °C/km geothermal gradient leads to
515 unrealistic trapping conditions for most veins. The broad variability of the oxygen isotope values
516 in type 1 calcite veins and the presence of low and high salinities in fluid inclusions can be
517 related to: (1) mixing of two fluids with inherently different compositions, or (2) presence of a
518 single external fluid, which was affected by variable amounts of fluid-rock interactions prior to
519 vein precipitation. In particular, high-salinity values and veins with oxygen isotopic composition
520 similar to that of the host rocks can be associated with: (1) a fluid of local origin, or (2) an
521 external fluid that became completely rock-buffered due to fluid-rock interactions prior to vein
522 precipitation. On the contrary, low-salinity values and veins with depleted oxygen isotope
523 compositions are associated with an external fluid affected by minor fluid-rock interactions. In

524 this view, the fluid associated with the precipitation of the most oxygen-depleted veins is the
525 least affected by local host-rock buffering or mixing with the local fluid, and the estimated
526 composition of such fluid can be used to estimate the isotopic composition of the external fluid.
527 Since direct microthermometry data are not available for veins with the most depleted oxygen
528 isotope values, the broad range of temperatures associated with all type 1 veins (i.e., 100–180
529 °C) can be used to estimate a fluid composition between 0‰ and +6‰ VSMOW (Fig. 12B). The
530 variability of Sr isotopes can be explained by a similar interpretation: The range of measured
531 values might be associated with an external fluid affected by varying degrees of rock buffering
532 prior to vein precipitation, or mixing of a local and an external fluid.

533 The third stage of carbonate precipitation is associated with type 2 calcite veins. The
534 absence of twinning in type 2 calcite crystals indicates that they have been affected by negligible
535 tectonic strain and supports their formation in a postkinematic setting, when the Tellaro
536 detachment fault system was no longer active and almost completely exhumed. Fluid inclusions
537 in type 2 calcite are monophasic at room temperature and do not allow determination of the
538 trapping temperature via traditional heating experiments. However, it can be proposed that such
539 monophasic inclusions are indicative of low-temperature precipitation ($T < 70$ °C) because: (1)
540 they are of the same size as the biphasic inclusions in other calcite veins, and (2) they did not
541 nucleate a vapor bubble after being at -20 °C for 2 wk (Goldstein and Reynolds, 1994). Such
542 trapping temperature would correspond to depth conditions between 2.5 km and the surface (Fig.
543 12A). In such a shallow environment, the zoned luminescence pattern common of type 2 calcite
544 (Fig. 6H) reflects the evolution from a dominant oxic environment (nonluminescent calcite) with
545 variation in the redox conditions (indicated by the tiny yellow subzones) to a suboxic
546 environment (yellow luminescent zone) and finally a reducing environment (dull luminescent

547 zone; Meyers, 1974, 1978). Within this framework, the tiny yellow zones in the dominant
548 nonluminescent zone have often been recorded from meteoric cements in the shallow
549 environment and reflect slight fluctuations in the redox conditions between oxic and suboxic
550 (e.g., Meyers, 1974, 1978).

551 The low salinity values corresponding to the measured high $T_{m\ ice}$ values are also
552 compatible with an ambient fluid of meteoric origin. Based on the stable isotope geochemistry,
553 type 2 calcite veins can be subdivided into two groups (Fig. 9C): (1) veins with depleted carbon
554 and moderately depleted oxygen ($-7\text{‰} < \delta^{13}\text{C} < +1\text{‰}$, $-7\text{‰} < \delta^{18}\text{O} < -4\text{‰}$ VPDB), and (2)
555 veins with enriched carbon and very depleted oxygen ($+1\text{‰} < \delta^{13}\text{C} < +3\text{‰}$, $-7\text{‰} < \delta^{18}\text{O} <$
556 -15‰ VPDB). In the first group of veins, low-temperature precipitation in a shallow
557 environment is suggested by: (1) the depleted carbon, indicative of precipitation from meteoric
558 water influenced by soil-derived CO_2 and the oxygen isotope values, aligned along the meteoric
559 alteration trend (Allan and Matthews, 1977; Videtich and Matthews, 1980). In the second group,
560 the rock-buffered carbon and the wide range of oxygen isotope composition indicate fluid-rock
561 interactions (Muechez et al., 1991; Walkden and Williams, 1991). The salinity of 0.7% wt. eq.
562 NaCl could be due to the interaction of the meteoric fluid (0% wt. eq. NaCl) with the host rock
563 (Verhaert et al., 2004).

564 In addition to the veining stages described earlier, the Tellaro detachment has also been
565 characterized by the development of tabular-shaped dolomite breccia bodies associated with
566 major low-angle fault segments (Figs. 4 and 5). Temperature-depth conditions of this
567 dolomitization event are not well constrained because crosscutting relationships between
568 dolomite (fluid stage 1) and calcite veining (fluid stage 2) are sparse and equivocal.
569 Nevertheless, dilational breccias are partially overprinted by tectonic stylolites and type 1 calcite

570 veins, suggesting that fault-related dolomitization occurred in relatively early deformation
571 phases.

572 **Synkinematic Orientation of the Fault System**

573 The Tellaro detachment is dissected by superimposed regional-scale high-angle faulting
574 and underwent more than 8 km of exhumation, which likely caused a postkinematic passive
575 rotation of both the low-angle fault zones and the associated subsidiary faults. The amount of
576 passive rotation is not fully constrained due to the lack of appropriate evidence for a
577 paleohorizontal reference surface. Nevertheless, the respective average attitude of major low-
578 angle and associated subsidiary high-angle faults can be used to estimate the original orientation
579 of the fault system and the amount of postkinematic passive rotation (e.g., Smith et al., 2007). In
580 the Tellaro detachment fault zone, the average dip of major low-angle faults is $\sim 10^\circ$ toward NE,
581 the average dip of subsidiary synthetic faults is $\sim 36^\circ$ toward the NE, and the average dip of
582 subsidiary antithetic faults is $\sim 76^\circ$ toward the SW (Fig. 13A). Restoring subsidiary faults to
583 conjugate pairs bisected by an assumed vertical principal axis of the regional stress ellipsoid
584 provides the maximum amount of possible passive tilting of $\sim 17^\circ$ toward the SW. This results in
585 an average dip of 25° toward the NE for the major low-angle fault segments during their activity
586 (Fig. 13B), a value that fits well into the range of low-angle normal faults described in
587 extensional continental settings worldwide, including the modern cases of the Corinth Gulf (e.g.,
588 Rietbrock et al., 1996), Papua New Guinea (e.g., Abers et al., 1997), and the Alto Tiberina fault
589 (e.g., Chiaraluce et al., 2007). However, simple shear models predict that the stress field in the
590 damage zone of a master slip surface has a maximum principal stress axis (σ_1) dipping toward
591 the tectonic transport direction by an angle between 45° and 90° (e.g., Logan et al., 1973).
592 Indeed, σ_1 results from the vectorial sum of the overburden load and a kinematically induced

593 stress associated with slip on the master slip surface (e.g., Storti et al., 2006). In the case of the
594 Tellaro detachment, this implies that: (1) the maximum principal axis of the stress ellipsoid
595 responsible for subsidiary faulting in the damage zone was dipping toward the NE; (2) the dip of
596 the southwestward-dipping antithetic faults was greater than that of the northeastward-dipping
597 ones; and (3) the average dip of major low-angle faults was lower than 25° during the main
598 kinematic activity.

599 **Inferences on Stress and Fluid Pressure Conditions**

600 To constrain the stress conditions required to develop specific deformation structures at
601 specific depths, traditional envelopes for extensional, hybrid, shear, and reshear failure can be
602 recalculated as functions of differential stress ($\delta\sigma$) and pore fluid factor (λ), and then plotted on
603 $\delta\sigma$ - λ diagrams (Cox, 2010). On such diagrams (Fig. 14A), differential stress and fluid pressure
604 conditions are represented by a point in the stable field (gray area). The point is moved upward
605 and rightward by increasing fluid pressure and differential stress, respectively, until one of the
606 failure envelopes is reached, and deformation occurs. As an example, for a fault with a
607 coefficient of friction similar to that of the host rock, oriented at 70° to the principal stress axis,
608 at 4 km depth: (1) slip along the misoriented fault surfaces is favored for $\lambda > 0.82$ and $\delta\sigma < 29$
609 MPa; (2) extensional failure in intact host rock is favored for $0.71 < \lambda < 0.82$ and $29 < \delta\sigma < 40$
610 MPa; (3) hybrid extensional-shear failure is favored for $0.64 < \lambda < 0.71$ and $40 < \delta\sigma < 48$ MPa;
611 and (4) shear failure along optimally oriented surfaces (subsidiary high-angle faults) is favored
612 for $\lambda < 0.64$ and $48 < \delta\sigma < 92$ MPa. Lower friction coefficients along the misoriented fault
613 surfaces (e.g., $\mu_s = 0.4$) favor slip of misoriented faults at lower fluid pressure factor ($\lambda > 0.55$)
614 and higher differential stress conditions ($\delta\sigma < 58$ MPa) but prevent extensional failure of the host
615 rock. Similar σ - λ diagrams can be plotted for the whole depth range associated with the main

616 kinematic activity of the Tellaro detachment, leading to comparable results (Fig. 14B). Fluid
617 pressures determined here are much higher than the hydrostatic fluid pressure ($\lambda = 0.4$) used for
618 the pressure correction of fluid inclusion microthermometry data (section 7.1 **[[Section numbers**
619 **are not used here. Please cite section title instead.]]**). However, it must be noted that the fluid
620 pressure estimations described here refer only to the moment when brittle fracturing occurs.
621 Immediately after fracturing, both the local stress field and the fluid pressure change. In
622 particular, fracturing leads to increased permeability (Figs. 14C and 14D), which is likely
623 associated with a fluid pressure drop (Fig. 14E). Precipitation of carbonate infilling in veins and
624 breccias occurs after such fluid pressure drop, at lower λ values. For this reason, the elevated
625 fluid pressure estimated for brittle fracturing cannot be used for correcting fluid inclusion
626 homogenization temperatures.

627 In the case where low-friction materials were not present along the misoriented fault
628 surfaces, friction along them would have been comparable to that of the host rock. Thus, slip
629 along the misoriented planes was made possible by elevated fluid pressure and low differential
630 stress conditions. Such conditions are confirmed by the aforementioned structural observations.
631 In particular: (1) veins and breccia textures indicate precipitation of carbonate cements into
632 voids, thus requiring elevated fluids pressures to sustain open fractures at depth (Sibson, 1990;
633 Cox, 1995); and (2) **there is evidence** of hydrofracturing processes, as indicated by the dilational
634 breccias (e.g., Sibson, 1986; Cosgrove, 1995; Woodcock et al., 2007, 2008), and the meshes of
635 irregular veins with curved short geometries and lack of systematic crosscutting relationships,
636 occurring in footwall damage zones of low-angle slip surfaces (Collettini et al., 2006a). Within
637 this framework, additional investigation of the dilational breccias is required to unravel possible
638 paleofluidization processes, analogous to what has been described by Smith et al. (2008) along

639 the Zuccale low-angle normal faults on Elba Island (Keller and Pialli, 1990), a few hundreds of
640 kilometers to the SE of Punta Bianca.

641 In addition to the brittle mechanics described here, ductile deformation processes were
642 also associated with the activity of the Tellaro detachment, as indicated by the S-C arrays of
643 tectonic stylolites developed in the limestones (Fig. 6A). Stress-driven pressure solution creep
644 processes likely weakened the fault zone, decreasing its frictional strength and favoring aseismic
645 slip (e.g., Mitterpergher et al., 2011) without preventing overpressure buildups. Indeed, the
646 leaching of the more soluble portions of the limestones by pressure dissolution leads to the
647 passive concentration of less permeable clayish materials, thus contributing to fault sealing and
648 local fluid overpressure during faulting.

649 **Permeability Creation and Reseal in the Fault Zone**

650 Microstructural and petrographic analyses of fault-related veins clearly indicate that veins
651 as thick as 1 cm opened by single-phase fracturing rather than incremental fragmentation and
652 crack widening (Oliver and Bons, 2001, and references therein). In particular, the absence of
653 fibrous infillings or crack-seal textures suggests that fracture opening rate was faster than
654 resealing due to mineral precipitation. Subsequently, circulating fluids precipitated carbonate
655 cements into the open spaces, leading to variable textures (e.g., equant granular, inequant
656 granular, or parallel comb), likely depending on fluid saturation and nucleation density
657 (Woodcock et al., 2007). Successive deformation pulses mostly opened new fractures rather than
658 reopening preexisting ones (Figs. 14C and 14D), suggesting that reseal hardening was associated
659 with cement precipitation and healing.

660 The lack of matrix and of evidence for crack-seal veining, and the mosaic to chaotic
661 texture indicate that dolomitic breccias can be classified as “implosion” or “dilation” breccias

662 according to available classifications (Sibson, 1986; Jébrak, 1997). In the Tellaro detachment
663 fault zone, limited rebrecciation of dolomitic breccias suggests that each body developed from a
664 single fracturing event, or from multiple fracturing events that followed each other in a short
665 time, before any carbonate precipitation could cement the clasts. We argue that the increased
666 fracture permeability in the breccia bodies was associated with fluid pressure drops, which
667 favored fluid circulation and saturation (Phillips, 1972), leading to the precipitation of dolomitic
668 cement into open voids. Eventually, cement precipitation caused reseal hardening of the
669 dolomitic breccia bodies, as testified by the almost complete absence of rebrecciation
670 (Woodcock et al., 2007). To explain why the dolomitic dilational breccias formed in localized
671 bodies, two hypotheses can be proposed. (1) Localized dolomite bodies could have formed
672 during incipient faulting, due to metasomatic limestone dolomitization associated with the
673 circulation of Mg-rich fluids along damage zones (Figs. 15A and 15B). Dolomitic bodies, more
674 rigid and less soluble than the surrounding limestones (Talman et al., 1990; Zhang et al., 2007),
675 influenced subsequent deformations (e.g., Mandl, 2000). In particular, limestone dissolution
676 could have favored stress concentration within the dolomitic bodies, promoting the localization
677 of brittle fracturing—and dilational brecciation—in the latter (Fig. 15C). (2) Alternatively,
678 dilational limestone breccia bodies could have initially formed at asperities along slip surfaces,
679 such as releasing or restraining bands, or in the process zone of propagating faults, due to local
680 stress concentrations (e.g., Sibson, 1986; Tarasewicz et al., 2005). Subsequently, pressure drops
681 associated with dilation and extensional fracturing promoted circulation of hydrothermal Mg-rich
682 fluids, which dolomitized the clasts and cemented the breccias. The former option seems to be
683 more appropriate for the Tellaro detachment dilation breccias, because: (1) fluid circulation was
684 calcite-dominated during most kinematic activity of the fault system, and, consequently, calcite-

685 cemented dilation breccias should have been more diffuse if brecciation occurred at fault
686 asperities; and (2) a gradient in clast dolomitization from the central to the marginal portions of
687 the breccias would have been expected if clast dolomitization occurred during breccia
688 cementation (e.g., Tarasewicz et al., 2005).

689 **Evolutionary Model**

690 Elevated fluid pressure conditions along the Tellaro detachment imply that it was a
691 “closed system,” at least on its upper boundary, without effective hydraulic connection to higher
692 structural levels or to the surface. Furthermore, isotopic signatures of the most oxygen-depleted
693 calcite veins and low salinity estimations from some microthermometry data indicate the
694 presence of an external fluid in the fault zone, implying an “open system” with effective
695 hydraulic connection with external reservoirs. In simple fault zone models, these two contrasting
696 hydraulic conditions fit within conduit-barrier architectures (Caine et al., 1996). Alternatively,
697 fault zone hydraulic properties may evolve through time during fault zone evolution (Brogi and
698 Novellino, 2015). The Tellaro detachment requires a more complex explanation, because these
699 two contrasting conditions are both observed in the footwall of the major low-angle fault zones
700 and characterize the main activity of the fault system. Transient permeability cycles,
701 characterized by low- and high-permeability stages alternating during the long-lasting activity of
702 the fault system, can reconcile the apparent contrasting structural and geochemical evidence. In
703 particular, during one cycle, fault-related veins and dilation breccias formed by a fracturing
704 pulse, causing secondary permeability creation, enhanced fluid flow, and fluid pressure drops.
705 This triggered reseal due to precipitation of carbonate cement. In a self-promoting process,
706 sealing-related fluid overpressure buildup favored slip along misoriented fault surfaces and a
707 new fracturing pulse. Several transient permeability cycles likely occurred during the long-

708 lasting evolution of the Tellaro detachment (Fig. 14E). We argue that rapid brittle fracturing
709 pulses were likely associated with co- and postseismic slip, while fracture reseal was slower,
710 likely occurring during interseismic periods (e.g., Sibson, 1990; Woodcock et al., 2007). Within
711 this framework, the composition of fluids precipitating carbonate veins in the fault zone evolved
712 through time (Fig. 15). Early fracturing and incipient faulting were characterized by rock-
713 buffered conditions at low total fluid flux, and favored localized dolomitization processes (Figs.
714 15A–15C). Far-sourced fluids, less affected by fluid-rock interactions, were present during the
715 main kinematic activity of the Tellaro detachment, when the fault system was able to connect
716 through the upper crust (Fig. 15D). Meteoric fluids dominated the postkinematic evolution of the
717 area (Fig. 15E).

718 **CONCLUSIONS**

719 The Tellaro detachment provides a well-exposed example of a low-angle extensional
720 fault system affecting carbonate rocks, active in late Miocene times during the progressive
721 exhumation of the Tuscan succession from ~8 km depth and ~190 °C peak conditions. The
722 original average dip of the principal slip zone of the Tellaro detachment is estimated to be lower
723 than 25° toward the NE, based on restoration of conjugate subsidiary fault pairs in damage
724 zones. As a consequence, our data support the activity of low-angle extensional fault zones as
725 pristine deformation structures, not affected by significant postkinematic passive rotation. Slip
726 on such a severely misoriented detachment was made possible by fluid overpressure buildups in
727 the footwall, as indicated by structural and microstructural evidence.

728 The Tellaro detachment was characterized by transient permeability cycles: Extensional
729 fracturing pulses created meshes of open fractures that favored fluid circulation in the fault zones
730 and mixing of local- and far-sourced fluids. Carbonate cement precipitation sealed the fractures,

731 reducing permeability and favoring episodic fluid overpressure buildups. Within this context, a
732 complex paleofluid evolution was associated with the long-lasting activity of the fault system
733 and was characterized by the precipitation of different generations of dolomite and calcite
734 infillings in dilation breccias and syntectonic veins, at gradually decreasing temperature and
735 depth conditions. In particular, initial incipient faulting was characterized by rock-buffered
736 conditions. Subsequently, fault zone propagation and linkage favored the development of an
737 “open system” environment, dominated by far-sourced fluids. Elevated fluid pressures and low
738 differential stress conditions favored repeated slip reactivation along the misoriented low-angle
739 principal slip zones and contributed to the opening of differently oriented veins in damage zones,
740 as well as hydrofracturing processes in the immediate proximity of the principal slip zones
741 themselves.

742 Results presented in this paper show that low-angle detachment can have remarkable
743 influence on fluid circulation within the upper crust, not only because of their combined conduit-
744 barrier hydraulic architecture, but also because fault zone permeability can be transient. Episodic
745 high- and low-permeability pulses can exist cyclically, **alternately** favoring fluid migration or
746 overpressure buildups. Characterization of these processes on exhumed field analogues has
747 implications in different fields, including a better understanding of low-angle normal faults
748 mechanics within the earthquake cycle, formation of ore deposits, and hydrocarbon migration
749 and trapping.

750 **ACKNOWLEDGMENTS**

751 This work has been supported by the Italian Ministry of Education, University, and
752 Research (MIUR) through PRIN project “La deformazione nelle rocce carbonatiche:
753 Implicazioni per la caratterizzazione e la modellizzazione dei serbatoi naturali di geofluidi”

754 (PRIN 2009, national coordinator E. Tondi, local coordinator F. Storti). Additional support
755 for the microthermometric study was given by the research grant OT/11/038 of the
756 Onderzoeksfonds KU Leuven. Thanks go also to: A. Comelli and L. Barchi (University of
757 Parma, Italy) for preparing thin sections and wafers; TS Lab & Geoservices (Pisa, Italy) for
758 preparing additional thin sections; H. Nijs (KU Leuven, Belgium) for polishing the thin
759 sections; M. Joachimski and colleagues (Friedrich-Alexander-Universität, Erlangen-
760 Nürnberg, Germany) for performing the oxygen and carbon stable isotope analysis; and A.
761 Kelly and V. Gallagher (**Scottish Universities Environmental Research Centre** [SUERC],
762 East Kilbride, Scotland) for performing the Sr isotope analysis. We are very grateful to Bob
763 Holdsworth and Stephen Cox for their constructive and helpful reviews that allowed us to
764 significantly improve the final manuscript, and to A. Hope Jahren and C. van Staal for their
765 editorial work.

766 **REFERENCES CITED** **[[Please spell out all journal titles/do not abbreviate.]]**

- 767 Abbate, E., Balestrieri, M.L., Bigazzi, G., Norelli, P., and Quercioli, C., 1994, Fission-track
768 dating and recent rapid denudation in Northern Apennines, Italy: *Memorie della Societa*
769 *Geologica Italiana*, v. 48, p. 579–585.
- 770 Abers, G.A., Mutter, C.Z., and Fang, J., 1997, Shallow dips of normal faults during rapid
771 extension: Earthquakes in the Woodlark-D'Entrecasteaux rift system, Papua New Guinea:
772 *Journal of Geophysical Research*, v. 102, p. 15,301–**15,317**, doi:10.1029/97JB00787.
- 773 Allan, J.R., and Matthews, R.K., 1977, Carbon and oxygen isotopes as diagenetic and
774 stratigraphic tools: Surface and subsurface data, Barbados, West Indies: *Geology*, v. 5,
775 p. 16–20, doi:10.1130/0091-7613(1977)5<16:CAOIAD>2.0.CO;2.

- 776 Anderson, E.M., 1951, The Dynamics of Faulting and Dyke Formations (2nd ed.): [\[\[City of](#)
777 [publication?\]\]](#), Oliver and Boyd, 206 p.
- 778 Argnani, A., 2002, The Northern Apennines and the kinematics of Europe-Africa convergence:
779 [Bollettino della Societa Geologica Italiana](#), v. 1, p. 47–60.
- 780 Axen, G.J., 1992, Pore pressure, stress increase, and fault weakening in low-angle normal
781 faulting: *Journal of Geophysical Research*, v. 97, p. 8979, doi:10.1029/92JB00517.
- 782 Bakker, R.J., 2003, Package FLUIDS 1. Computer programs for analysis of fluid inclusion data
783 and for modelling bulk fluid properties: *Chemical Geology*, v. 194, p. 3–23,
784 doi:10.1016/S0009-2541(02)00268-1.
- 785 Balestrieri, M.L., Bernet, M., Brandon, M.T., Picotti, V., Reiners, P., and Zattin, M., 2003,
786 Pliocene and Pleistocene exhumation and uplift of two key areas of the Northern Apennines:
787 *Quaternary International*, v. 101–102, p. 67–73, doi:10.1016/S1040-6182(02)00089-7.
- 788 Barchi, M.R., Minelli, G., and Piali, G., 1998, The CROP 03 Profile: A synthesis of results on
789 deep structures of the Northern Apennines: *Memorie della Societa Geologica Italiana*, v. 52,
790 p. 383–400.
- 791 Bebout, G.E., Anastasio, D.J., and Holl, J.E., 2001, Synorogenic crustal fluid infiltration in the
792 Idaho-Montana thrust belt: *Geophysical Research Letters*, v. 28, p. 4295–4298,
793 doi:10.1029/2001GL013711.
- 794 Bernet, M., Brandon, M.T., Garver, J.I., and Molitor, B.R., 2004, Fundamentals of detrital zircon
795 fission-track analysis for provenance and exhumation studies with examples from the
796 European Alps, *in* Bernet, M., and Spiegel, C., eds., *Detrital Thermochronology;*
797 *Provenance Analysis, Exhumation, and Landscape Evolution of Mountain Belts*: Geological
798 Society of America Special Paper 378, p. 25–36.

- 799 **[[Reference "Bernini et al., 1990" not in text.]]**Bernini, M., Boccaletti, M., Moratti, G.,
800 Papani, G., Sani, F., and Torelli, L., 1990, Episodi compressivi neogenico-quadernari
801 nell'area estensionale tirrenica nord-orientale. Dati in mare e a terra: Memorie della Societa
802 Geologica Italiana, v. 45, p. 577–589.
- 803 Boccaletti, M., Elter, P., and Guazzone, G., 1971, Plate tectonic models for the development of
804 the western Alps and Northern Apennines: *Nature*, v. 234, p. 108–111.
- 805 Boccaletti, M., Corti, G., and Martelli, L., 2011, Recent and active tectonics of the external zone
806 of the Northern Apennines (Italy): *International Journal of Earth Sciences*, v. 100, p. 1331–
807 1348, doi:10.1007/s00531-010-0545-y.
- 808 Bodnar, R.J., 1993, Revised equation and table for determining the freezing point depression of
809 H₂O-NaCl solutions: *Geochimica et Cosmochimica Acta*, v. 57, p. 683–684,
810 doi:10.1016/0016-7037(93)90378-A.
- 811 Bonini, M., Moratti, G., Sani, F., and Balestrieri, M.L., 2013, Compression-to-extension record
812 in the late Pliocene–Pleistocene Upper Valdarno Basin (Northern Apennines, Italy):
813 Structural and thermochronological constraints: *Italian Journal of Geosciences*, v. 132,
814 p. 54–80, doi:10.3301/IJG.2011.18.
- 815 Bradshaw, G.A., and Zoback, M.D., 1988, Listric normal faulting, stress refraction, and the state
816 of stress in the Gulf Coast basin: *Geology*, v. 16, p. 271–274, doi:10.1130/0091-
817 7613(1988)016<0271:LNFSRA>2.3.CO;2.
- 818 Brogi, A., 2004, Assetto geologico del nucleo di Falda Toscana affiorante nel settore occidentale
819 del Monte Amiata (Appennino Settentrionale): Strutture pre- e sin-collisionali relitte
820 preservate durante lo sviluppo della tettonica distensiva post-collisionale: *Bollettino della*
821 *Societa Geologica Italiana*, v. 123, p. 443–461.

- 822 Brogi, A., 2008, Kinematics and geometry of Miocene low-angle detachments and exhumation
823 of the metamorphic units in the hinterland of the Northern Apennines (Italy): Journal of
824 Structural Geology, v. 30, p. 2–20, doi:10.1016/j.jsg.2007.09.012.
- 825 Brogi, A., and Liotta, D., 2006, Understanding the crustal structures of southern Tuscany: The
826 contribution of the CROP18 Project: *Bollettino di Geofisica Teorica ed Applicata*, v. 47, p.
827 401–423.
- 828 Brogi, A., and Novellino, R., 2015, Low angle normal fault (LANF) zone architecture and
829 permeability features in bedded carbonate from inner Northern Apennines (Rapolano Terme,
830 central Italy): *Tectonophysics*, v. 638, p. 126–146, doi:10.1016/j.tecto.2014.11.005.
- 831 Buck, W.R., 1991, Modes of continental lithospheric extension: *Journal of Geophysical*
832 *Research*, v. 96, p. 20,161–20,178, doi:10.1029/91JB01485.
- 833 Burkhard, M., 1993, Calcite twins, their geometry, appearance and significance as stress-strain
834 markers and indicators of tectonic regime: A review: *Journal of Structural Geology*, v. 15,
835 p. 351–368, doi:10.1016/0191-8141(93)90132-T.
- 836 Byerlee, J., 1978, Friction of rocks: *Pure and Applied Geophysics*, v. 116, p. 615–626,
837 doi:10.1007/BF00876528.
- 838 Caine, J.S., Evans, J.P., and Forster, C.B., 1996, Fault zone architecture and permeability
839 structure: *Geology*, v. 24, p. 1025–1028, doi:10.1130/0091-
840 7613(1996)024<1025:FZAAPS>2.3.CO;2.
- 841 Carlini, M., Artoni, A., Aldega, L., Balestrieri, M.L., Corrado, S., Vescovi, P., Bernini, M., and
842 Torelli, L., 2013, Exhumation and reshaping of far-travelled/allochthonous tectonic units in
843 mountain belts. New insights for the relationships between shortening and coeval extension

- 844 in the western Northern Apennines (Italy): *Tectonophysics*, v. 608, p. 267–287,
845 doi:10.1016/j.tecto.2013.09.029.
- 846 Carmignani, L., and Kligfield, R., 1990, Crustal extension in the Northern Apennines: The
847 transition from compression to extension in the Alpi Apuane core complex: *Tectonics*, v. 9,
848 p. 1275–1303, doi:10.1029/TC009i006p01275.
- 849 Carmignani, L., Decandia, F.A., Fantozzi, P.L., Lazzarotto, A., Liotta, D., and Meccheri, M.,
850 1994, Tertiary extensional tectonics in Tuscany (Northern Apennines, Italy):
851 *Tectonophysics*, v. 238, p. 295–315, doi:10.1016/0040-1951(94)90061-2.
- 852 Carmignani, L., Decandia, F.A., Disperati, L., Fantozzi, P.L., Lazzarotto, A., Liotta, D., and
853 Oggiano, G., 1995, Relationships between the Tertiary structural evolution of the Sardinia-
854 Corsica-Provençal Domain and the Northern Apennines: *Terra Nova* (Helsinki, Finland), v.
855 7, no. 2, p. 128–137.
- 856 Carosi, R., Leoni, L., Montomoli, C., and Sartori, F., 2003, Very low-grade metamorphism in the
857 Tuscan Nappe, Northern Apennines, Italy: Relationships between deformation and
858 metamorphic indicators in the La Spezia mega-fold: *Swiss Bulletin of Mineralogy and*
859 *Petrology*, v. 83, p. 18.
- 860 Carta Geologica d'Italia, 2005, Foglio 248 “La Spezia”: Roma, Italy, Servizio Geologico
861 d'Italia, **scale** 1:50,000.
- 862 Carter, K.E., and Dworkin, S.I., 1990, Channelized fluid flow through shear zones during fluid-
863 enhanced dynamic recrystallization, Northern Apennines, Italy: *Geology*, v. 18, p. 720–723,
864 doi:10.1130/0091-7613(1990)018<0720:CFFTSZ>2.3.CO;2.
- 865 Cerrina Feroni, A.G., Plesi, G., Fanelli, G., Leoni, L., and Martinelli, P., 1983, Contributo alla
866 conoscenza dei processi metamorfici di grado molto basso (anchi-metamorfismo) a carico

- 867 della falda toscana nell'area del ricoprimento Apuano: Bollettino della Societa Geologica
868 Italiana, v. 102, p. 269–280.
- 869 Chester, F.M., and Logan, J.M., 1986, Implications for mechanical properties of brittle faults
870 from observations of the Punchbowl fault zone, California: Pure and Applied Geophysics,
871 v. 124, p. 79–106, doi:10.1007/BF00875720.
- 872 Chiaraluce, L., Chiarabba, C., Collettini, C., Piccinini, D., and Cocco, M., 2007, Architecture
873 and mechanics of an active low-angle normal fault: Alto Tiberina fault, Northern Apennines,
874 Italy: Journal of Geophysical Research, v. 112, B10310, doi:10.1029/2007JB005015.
- 875 Clemenzi, L., Molli, G., Storti, F., Mucchez, P., Swennen, R., and Torelli, L., 2014, Extensional
876 deformation structures within a convergent orogen: The Val di Lima low-angle normal fault
877 system (Northern Apennines, Italy): Journal of Structural Geology, v. 66, p. 205–222,
878 doi:10.1016/j.jsg.2014.05.019.
- 879 Collettini, C., 2011, The mechanical paradox of low-angle normal faults: Current understanding
880 and open questions: Tectonophysics, v. 510, p. 253–268, doi:10.1016/j.tecto.2011.07.015.
- 881 Collettini, C., and Holdsworth, R.E., 2004, Fault zone weakening and character of slip along
882 low-angle normal faults: Insights from the Zuccale fault, Elba, Italy: Journal of the
883 Geological Society of London, v. 161, p. 1039–1051, doi:10.1144/0016-764903-179.
- 884 **[[Reference "Collettini and Sibson, 2001" not in text.]]** Collettini, C., and Sibson, R.H., 2001,
885 Normal faults, normal friction?: Geology, v. 29, p. 927–930, doi:10.1130/0091-
886 7613(2001)029<0927:NFNF>2.0.CO;2.
- 887 Collettini, C., De Paola, N., and Goultly, N.R., 2006a, Switches in the minimum compressive
888 stress direction induced by overpressure beneath a low-permeability fault zone: Terra Nova
889 (Helsinki, Finland), v. 18, no. 3, p. 224–231, doi:10.1111/j.1365-3121.2006.00683.x.

- 890 Collettini, C., De Paola, N., Holdsworth, R.E., and Barchi, M.R., 2006b, The development and
891 behaviour of low-angle normal faults during Cenozoic asymmetric extension in the Northern
892 Apennines, Italy: *Journal of Structural Geology*, v. 28, p. 333–352,
893 doi:10.1016/j.jsg.2005.10.003.
- 894 Cosgrove, J.W., 1995, The expression of hydraulic fracturing in rocks and sediments, *in Ameen,*
895 *M.S., ed., Fractography: Fracture Topography as a Tool in Fracture Mechanics and Stress*
896 *Analysis*: Geological Society of London Special Publication 92, p. 187–196,
897 doi:10.1144/GSL.SP.1995.092.01.10.
- 898 Cox, S.F., 1995, Faulting processes at high fluid pressures: An example of fault valve behaviour
899 from the Wattle Gully fault, Victoria, Australia: *Journal of Geophysical Research*, v. 100,
900 p. 12,841–12,859, doi:10.1029/95JB00915.
- 901 Cox, S.F., 2010, The application of failure mode diagrams for exploring the roles of fluid
902 pressure and stress states in controlling styles of fracture-controlled permeability
903 enhancement in faults and shear zones: *Geofluids*, v. 10, p. 217–233, doi:10.1111/j.1468-
904 8123.2010.00281.x.
- 905 Dahlen, F., 1990, Critical taper model of fold-and-thrust belts and accretionary wedges: *Annual*
906 *Review of Earth and Planetary Sciences*, v. 18, p. 55–99,
907 doi:10.1146/annurev.ea.18.050190.000415.
- 908 Dahlen, F.A., Suppe, J., and Davis, D., 1984, Mechanics of fold-and-thrust belts and accretionary
909 wedges: Cohesive Coulomb theory: *Journal of Geophysical Research*, v. 89, p. 10,087–
910 10,101, doi:10.1029/JB089iB12p10087.

- 911 Davis, D., Suppe, J., and Dahlen, F.A., 1983, Mechanics of fold-and-thrust belts and accretionary
912 wedges: *Journal of Geophysical Research*, v. 88, p. 1153–1172,
913 doi:10.1029/JB088iB02p01153.
- 914 Decandia, F.A., Lazzarotto, A., and Liotta, D., 1998, The CROP 03 traverse: Insights on post-
915 collisional evolution of Northern Apennines: *Memorie della Societa Geologica Italiana*,
916 v. 52, p. 427–440.
- 917 Dewey, J.F., Helman, M.L., Knott, S.D., Turco, E., and Hutton, D.H.W., 1989, Kinematics of the
918 western Mediterranean, *in Coward, M.P., Dietrich, D., and Park, R.G., eds., Alpine*
919 *Tectonics*: Geological Society of London Special Publication 45, p. 265–283,
920 doi:10.1144/GSL.SP.1989.045.01.15.
- 921 Di Pisa, A., Franceschelli, M., Leoni, L., and Meccheri, M., 1985, Regional variation of the
922 metamorphic temperatures across the Tuscanid 1 unit and its implications on the alpine
923 metamorphism (Apuane Alps, N-Tuscany): *Neues Jahrbuch für Mineralogie, Abhandlungen*,
924 v. 151, p. 197–211.
- 925 Doglioni, C., 1991, A proposal for the kinematic modelling of W-dipping subductions—Possible
926 applications to the Tyrrhenian-Apennines system: *Terra Nova* (Helsinki, Finland), v. 3,
927 no. 4, p. 423–434, doi:10.1111/j.1365-3121.1991.tb00172.x.
- 928 Elter, P., 1975, Introduction à la géologie de l'Apennin septentrional: *Bulletin de la Societe*
929 *Geologique de France*, ser. 7, v. XVII, p. 956–962, doi:10.2113/gssgfbull.S7-XVII.6.956.
- 930 Elter, P., and Pertusati, P., 1973, Considerazioni sul limite Alpi-Appennino e sulle relazioni con
931 l'arco delle Alpi occidentali: *Memorie della Societa Geologica Italiana*, v. 12, p. 359–375.

- 932 Elter, P., Giglia, G., Tongiorgi, M., and Trevisan, L., 1975, Tensional and compressional areas in
933 the recent (Tortonian to present) evolution of the Northern Apennines: *Bollettino di*
934 *Geofisica Teorica ed Applicata*, v. 17, p. 3–18.
- 935 Fagereng, Å., Remitti, F., and Sibson, R.H., 2010, Shear veins observed within anisotropic fabric
936 at high angles to the maximum compressive stress: *Nature Geoscience*, v. 3, p. 482–485,
937 doi:10.1038/ngeo898.
- 938 **[[Reference "Federici, 1973" not in text.]]**Federici, P.R., 1973, La tettonica recente
939 dell'Appennino: 1. Il bacino villafranchiano di Sarzana e il suo significato nel quadro dei
940 movimenti distensivi a nord-ovest delle Alpi Apuane: *Bollettino della Societa Geologica*
941 *Italiana*, v. 92, p. 287–301.
- 942 Federici, P.R., and Raggi, G., 1975, Una nuova interpretazione della tettonica dei monti della
943 Spezia: *Bollettino della Societa Geologica Italiana*, v. 94, p. 945–960.
- 944 **[[Reference "Federici and Rau, 1980" not in text. Add citation or delete here. Spell out P.**
945 **F. Geodin.]]**Federici, P.R., and Rau, A., 1980, Note illustrative della neotettonica del Foglio
946 96-Massa: *P. F. Geodin.* v. 356, p. 1365–1382.
- 947 Fellin, M.G., Reiners, P.W., Brandon, M.T., Wüthrich, E., Balestrieri, M.L., and Molli, G., 2007,
948 Thermochronologic evidence for the exhumational history of the Alpi Apuane metamorphic
949 core complex, Northern Apennines, Italy: *Tectonics*, v. 26, TC6015,
950 doi:10.1029/2006TC002085.
- 951 Franceschelli, M., Leoni, L., Memmi, I., and Puxeddu, M., 1986, Regional distribution of Al-
952 silicates and metamorphic zonation in the low-grade Verrucano metasediments from the
953 Northern Apennines, Italy: *Journal of Metamorphic Geology*, v. 4, p. 309–321,
954 doi:10.1111/j.1525-1314.1986.tb00353.x.

- 955 Fricke, H.C., Wickham, S.M., and O'Neil, J.R., 1992, Oxygen and hydrogen isotope evidence
956 for meteoric water infiltration during mylonitization and uplift in the Ruby Mountains–East
957 Humboldt Range core complex, Nevada: *Contributions to Mineralogy and Petrology*, v. 111,
958 p. 203–221, doi:10.1007/BF00348952.
- 959 Friedman, I., and O'Neil, J.R., 1977, Compilation of stable isotope fractionation factors of
960 geochemical interest, in **Fleisher, M., ed.**, *Data of Geochemistry* (6th ed.): U.S. Geological
961 Survey Professional Paper 440-KK, 117 p.
- 962 G ebelin, A., Mulch, A., Teyssier, C., Heizler, M., Vennemann, T., and Seaton, N.C.A., 2011,
963 Oligo-Miocene extensional tectonics and fluid flow across the Northern Snake Range
964 detachment system, Nevada: *Tectonics*, v. 30, TC5010, doi:10.1029/2010TC002797.
- 965 Goldstein, R.H., and Reynolds, J., 1994, *Systematics of Fluid Inclusions in Diagenetic Minerals*:
966 Society for Sedimentary Geology, Short Course Notes 31, 199 p., doi:10.2110/scn.94.31.
- 967 Gottardi, R., Teyssier, C., Mulch, A., Vennemann, T.W., and Wells, M.L., 2011, Preservation of
968 an extreme transient geotherm in the Raft River detachment shear zone: *Geology*, v. 39,
969 p. 759–762, doi:10.1130/G31834.1.
- 970 Gratier, J.-P., Richard, J., Renard, F., Mittempergher, S., Doan, M.-L., Di Toro, G., Hadizadeh,
971 J., and Boullier, A.-M., 2011, Aseismic sliding of active faults by pressure solution creep:
972 Evidence from the San Andreas fault observatory at depth: *Geology*, v. 39, p. 1131–1134,
973 doi:10.1130/G32073.1.
- 974 Gratier, J.-P., Dysthe, D.K., and Renard, F., 2013, Chapter 2—The role of pressure solution
975 creep in the ductility of the Earth's upper crust: *Advances in Geophysics*, v. 54, p. 47–179,
976 doi:10.1016/B978-0-12-380940-7.00002-0.

- 977 Gray, D.R., Gregory, R.T., and Durney, D.W., 1991, Rock-buffered fluid-rock interaction in
978 deformed quartz-rich turbidite sequences, eastern Australia: *Journal of Geophysical*
979 *Research*, v. 96, p. 19,681–19,704, doi:10.1029/91JB01639.
- 980 Gudmundsson, A., 2001, Fluid overpressure and flow in fault zones: Field measurements and
981 models: *Tectonophysics*, v. 336, p. 183–197, doi:10.1016/S0040-1951(01)00101-9.
- 982 Hacker, B.R., 1997, Diagenesis and fault valve seismicity of crustal faults: *Journal of*
983 *Geophysical Research*, v. 102, no. 11, p. 24,459–24,467, doi:10.1029/97JB02025
- 984 Hubbert, M.K., Rubey, W.W., 1959, Role of fluid pressure in mechanics of overthrust faulting: I.
985 Mechanics of fluid-filled porous solids and its application to overthrust faulting: *Geological*
986 *Society of America Bulletin*, v. 70, p. 115–166.
- 987 Ingebritsen, S.E., and Manning, C.E., 2010, Permeability of the continental crust: Dynamic
988 variations inferred from seismicity and metamorphism: *Geofluids*, v. 10, p. 193–205,
989 doi:10.1111/j.1468-8123.2010.00278.x.
- 990 Jébrak, M., 1997, Hydrothermal breccias in vein-type ore deposits: A review of mechanisms,
991 morphology and size distribution: *Ore Geology Reviews*, v. 12, p. 111–134,
992 doi:10.1016/S0169-1368(97)00009-7.
- 993 Jolivet, L., Faccenna, C., Goffé, B., Mattei, M., Rossetti, F., Brunet, C., Storti, F., Funicello, R.,
994 Cadet, J.P., D'Agostino, N., and Parra, T., 1998, Midcrustal shear zones in postorogenic
995 extension: Example from the northern Tyrrhenian Sea: *Journal of Geophysical Research*,
996 v. 103, p. 12,123–12,160, doi:10.1029/97JB03616.
- 997 Keller, J.V.A., and Pialli, G., 1990, Tectonics of the island of Elba: A reappraisal: *Bollettino*
998 *della Società Geologica Italiana*, v. 109, p. 413–425.

- 999 Kirschner, D.L., and Kennedy, L., 2001, Limited syntectonic fluid flow in carbonate hosted
1000 thrust faults of the Front Ranges, Canadian Rockies, inferred from stable isotope data and
1001 structures: *Journal of Geophysical Research*, v. 106, p. 8827–8840,
1002 doi:10.1029/2000JB900414.
- 1003 Lacroix, B., Leclère, H., Buatier, M., and Fabbri, O., 2013, Weakening processes in thrust faults:
1004 Insights from the Monte Perdido thrust fault (southern Pyrenees, Spain): *Geofluids*, v. 13,
1005 p. 56–65, doi:10.1111/gfl.12010.
- 1006 Laubach, S.E., Eichhubl, P., Hilgers, C., and Lander, R.H., 2010, Structural diagenesis: *Journal*
1007 *of Structural Geology*, v. 32, p. 1866–1872, doi:10.1016/j.jsg.2010.10.001.
- 1008 Lavier, L.L., and Roger Buck, W., 2002, Half graben versus large-offset low-angle normal fault:
1009 Importance of keeping cool during normal faulting: *Journal of Geophysical Research*,
1010 v. 107, **no. B6, p. ETG 8-1–ETG 8-13**, doi:10.1029/2001JB000513.
- 1011 Lavier, L.L., Roger Buck, W., and Poliakov, A.N.B., 1999, Self-consistent rolling-hinge model
1012 for the evolution of large-offset low-angle normal faults: *Geology*, v. 27, p. 1127–1130,
1013 doi:10.1130/0091-7613(1999)027<1127:SCRHMF>2.3.CO;2.
- 1014 Lister, G.S., Etheridge, M.A., and Symonds, P.A., 1986, Detachment faulting and the evolution
1015 of passive continental margins: *Geology*, v. 14, p. 246–250, doi:10.1130/0091-
1016 7613(1986)14<246:DFATEO>2.0.CO;2.
- 1017 Logan, J.M., Iwasaki, T., Friedman, M., and Kling, S.A., 1973, Experimental investigations of
1018 sliding friction in multilithologic specimens, *in* Picus, H., ed., *Geological Factors in Rapid*
1019 *Excavation: Geological Society of America Engineering Geology Case Histories*, v. 9, p.
1020 55–67.

- 1021 Malinverno, A., and Ryan, W.B.F., 1986, Extension in the Tyrrhenian Sea and shortening in the
1022 Apennines as result of arc migration driven by sinking of the lithosphere: *Tectonics*, v. 5,
1023 p. 227–245, doi:10.1029/TC005i002p00227.
- 1024 Mandl, G., 2000, *Faulting in Brittle Rocks: An Introduction to the Mechanics of Tectonic Faults*:
1025 [\[\[city of publication?\]\]](#), Springer, 434 p.
- 1026 [\[\[Reference "Martini et al., 2011" not in text.\]\]](#) Martini, I.P., Sagri, M., and Colella, A., 2011.
1027 Neogene-Quaternary basins of the inner Apennines and Calabrian arc, *in* Vai, G.B., and
1028 Martini, I.P., eds., *Anatomy of an Orogen: The Apennines and Adjacent Mediterranean*
1029 *Basins*: [\[\[city of publication?\]\]](#) Netherlands, Springer, p. 375–399.
- 1030 McArthur, J.M., Howarth, R.J., and Bailey, T.R., 2001, Strontium isotope stratigraphy:
1031 LOWESS version 3: Best fit to the marine Sr-isotope curve for 0–509 Ma and
1032 accompanying look-up table for deriving numerical age: *The Journal of Geology*, v. 109,
1033 p. 155–170, doi:10.1086/319243.
- 1034 Melosh, H.J., 1990, Mechanical basis for low-angle normal faulting in the Basin and Range
1035 Province: *Nature*, v. 343, p. 331–335, doi:10.1038/343331a0.
- 1036 Meyers, W.J., 1974, Carbonate cement stratigraphy of the Lake Valley Formation
1037 (Mississippian) Sacramento Mountains, New Mexico: *Journal of Sedimentary Petrology*,
1038 v. 44, p. 837–861.
- 1039 Meyers, W.J., 1978, Carbonate cements: Their regional distribution and interpretation in
1040 Mississippian limestones, New Mexico, *in* Schneidermann, N., and Harris, P.M., eds.,
1041 *Carbonate Cements: Society of Economic Paleontologists and Mineralogists Special*
1042 *Publication 36*, p. 223–229.

- 1043 Miller, S.A., Collettini, C., Chiaraluce, L., Cocco, M., Barchi, M., and Kaus, B.J.P., 2004,
1044 Aftershocks driven by a high-pressure CO₂ source at depth: *Nature*, v. 427, p. 724–727,
1045 doi:10.1038/nature02251.
- 1046 Mittempergher, S., Di Toro, G., Gratier, J.P., Hadizadeh, J., Smith, S.A.F., and Spiess, R., 2011,
1047 Evidence of transient increases of fluid pressure in SAFOD phase III cores: *Geophysical*
1048 *Research Letters*, v. 38, L03301, doi:10.1029/2010GL046129.
- 1049 Molli, G., 2008, Northern Apennine–Corsica orogenic system: An updated overview, *in*
1050 *Siegesmund, S., Fügenschuh, B., and Froitzheim, M., eds., Tectonic Aspects of the Alpine-*
1051 *Dinaride-Carpathian System*: Geological Society of London Special Publication 298,
1052 p. 413–442, doi:10.1144/SP298.19.
- 1053 Molli, G., Conti, P., Giorgetti, G., Meccheri, M., and Oesterling, N., 2000a, Microfabric study on
1054 the deformational and thermal history of the Alpi Apuane marbles (Carrara marbles), Italy:
1055 *Journal of Structural Geology*, v. 22, p. 1809–1825, doi:10.1016/S0191-8141(00)00086-9.
- 1056 Molli, G., Giorgetti, G., and Meccheri, M., 2000b, Structural and petrological constraints on the
1057 tectono-metamorphic evolution of the Massa unit (Alpi Apuane, NW Tuscany, Italy):
1058 *Geological Journal*, v. 35, p. 251–264, doi:10.1002/gj.860.
- 1059 Molli, G., Giorgetti, G., and Meccheri, M., 2002, Tectono-metamorphic evolution of the Alpi
1060 Apuane metamorphic complex: New data and constraints for geodynamic models: *Bollettino*
1061 *della Societa Geologica Italiana*, v. 121, p. 789–800.
- 1062 Molli, G., White, J.C., Kennedy, L., and Taini, V., 2011, Low-temperature deformation of
1063 limestone, Isola Palmaria, Northern Apennine, Italy—The role of primary textures,
1064 precursory veins and intracrystalline deformation in localization: *Journal of Structural*
1065 *Geology*, v. 33, p. 255–270, doi:10.1016/j.jsg.2010.11.015.

- 1066 Montomoli, C., 2002, Vein development and fluid inclusion data: Insight on the evolution of the
1067 Tuscan Nappe in the Northern Apennine: *Bollettino della Societa Geologica Italiana*, v. 1,
1068 Special Issue, p. 801–817.
- 1069 Montomoli, C., Ruggieri, G., Boiron, M.C., and Cathelineau, M., 2001, Pressure fluctuation
1070 during uplift of the Northern Apennines (Italy): A fluid inclusions study: *Tectonophysics*,
1071 v. 341, p. 121–139, doi:10.1016/S0040-1951(01)00197-4.
- 1072 Moore, J.C., and Vrolijk, P., 1992, Fluids in accretionary prisms: *Reviews of Geophysics*, v. 30,
1073 p. 113–135, doi:10.1029/92RG00201.
- 1074 **[[Reference "Moretti, 1992" not in text.]]** Moretti, A., 1992, Evoluzione tettonica della
1075 Toscana settentrionale tra il Pliocene e l'Olocene: *Bollettino della Societa Geologica*
1076 *Italiana*, v. 111, p. 459–492.
- 1077 Morrison, J., 1994, Meteoric water-rock interaction in the lower plate of the Whipple Mountain
1078 metamorphic core complex, California: *Journal of Metamorphic Geology*, v. 12, p. 827–840,
1079 doi:10.1111/j.1525-1314.1994.tb00062.x.
- 1080 Morrison, J., and Anderson, J., 1998, Footwall refrigeration along a detachment fault:
1081 Implications for the thermal evolution of core complexes: *Science*, v. 279, no. 5347, p. 63–
1082 66.
- 1083 Muechez, P., Viaene, W., and Marshall, J.D., 1991, Origin of shallow burial cements in the late
1084 Viséan of the Campine Basin, Belgium: *Sedimentary Geology*, v. 73, p. 257–271,
1085 doi:10.1016/0037-0738(91)90088-U.
- 1086 Muechez, P., Slobodnik, M., Viaene, W.A., and Keppens, E., 1995, Geochemical constraints on
1087 the origin and migration of palaeofluids at the northern margin of the Variscan foreland,

- 1088 southern Belgium: *Sedimentary Geology*, v. 96, p. 191–200, doi:10.1016/0037-
1089 0738(94)00118-E.
- 1090 Mulch, A., Teyssier, C., Cosca, M.A., Vanderhaeghe, O., and Vennemann, T.W., 2004,
1091 Reconstructing paleoelevation in eroded orogens: *Geology*, v. 32, p. 525–528,
1092 doi:10.1130/G20394.1.
- 1093 Mulch, A., Teyssier, C., Cosca, M.A., and Vennemann, T.W., 2006, Thermomechanical analysis
1094 of strain localization in a ductile detachment zone: *Journal of Geophysical Research*, v. 111,
1095 B12405, doi:10.1029/2005JB004032.
- 1096 Oliver, N.H.S., and Bons, P.D., 2001, Mechanisms of fluid flow and fluid-rock interaction in
1097 fossil metamorphic hydrothermal systems inferred from vein-wallrock patterns, geometry
1098 and microstructure: *Geofluids*, v. 1, p. 137–162, doi:10.1046/j.1468-8123.2001.00013.x.
- 1099 Passchier, C.W., and Trouw, R.A.J., 2005, *Microtectonics*: [\[\[city of publication?\]\]](#) Springer,
1100 366 p.
- 1101 Patacca, E., Sartori, R., and Scandone, P., 1990, Tyrrhenian Basin and Apenninic arc: Kinematic
1102 relations since late Tortonian times: *Memorie della Societa Geologica Italiana*, v. 45,
1103 p. 425–451.
- 1104 Person, M., Mulch, A., Teyssier, C., and Gao, Y., 2007, Isotope transport and exchange within
1105 metamorphic core complexes: *American Journal of Science*, v. 307, p. 555–589,
1106 doi:10.2475/03.2007.01.
- 1107 Phillips, W.J., 1972, Hydraulic fracturing and mineralization: *Journal of the Geological Society*
1108 of London, v. 128, p. 337–359, doi:10.1144/gsjgs.128.4.0337.

- 1109 Ranero, C.R., and Pérez-Gussinyé, M., 2010, Sequential faulting explains the asymmetry and
1110 extension discrepancy of conjugate margins: *Nature*, v. 468, p. 294–299,
1111 doi:10.1038/nature09520.
- 1112 Reutter, K.-J., Teichmüller, M., Teichmüller, R., and Zanzucchi, G., 1983, The coalification
1113 pattern in the Northern Apennines and its palaeo-geothermic and tectonic significance:
1114 *Geologische Rundschau*, v. 72, p. 861–893, doi:10.1007/BF01848346.
- 1115 Rietbrock, A., Tiberi, C., Scherbaum, F., and Lyon-Caen, H., 1996, Seismic slip on a low angle
1116 normal fault in the Gulf of Corinth: Evidence from high-resolution cluster analysis of
1117 microearthquakes: *Geophysical Research Letters*, v. 23, p. 1817–1820,
1118 doi:10.1029/96GL01257.
- 1119 Rossetti, F., Balsamo, F., Villa, I.M., Bouybaouenne, M., Faccenna, C., and Funiciello, R., 2008,
1120 Pliocene–Pleistocene HT-LP metamorphism during multiple granitic intrusions in the
1121 southern branch of the Larderello geothermal field (southern Tuscany, Italy): *Journal of the*
1122 *Geological Society of London*, v. 165, p. 247–262, doi:10.1144/0016-76492006-132.
- 1123 Rossetti, F., Aldega, L., Tecce, F., Balsamo, F., Billi, A., and Brilli, M., 2011, Fluid flow within
1124 the damage zone of the Boccheggiano extensional fault (Larderello-Travale geothermal
1125 field, central Italy): Structures, alteration and implications for hydrothermal mineralization
1126 in extensional settings: *Geological Magazine*, v. 148, p. 558–579,
1127 doi:10.1017/S001675681000097X.
- 1128 Royden, L., 1988, Flexural behavior of the continental lithosphere in Italy: Constraints imposed
1129 by gravity and deflection data: *Journal of Geophysical Research*, v. 93, p. 7747–7766,
1130 doi:10.1029/JB093iB07p07747.

- 1131 Salvini, F., 2014, Daisy3: The Structural Data Integrated System Analyser:
1132 <http://host.uniroma3.it/progetti/fralab> (accessed). **[[Please list date site was last accessed.]]**
- 1133 Scott, R.J., and Lister, G.S., 1992, Detachment faults: Evidence for a low-angle origin: *Geology*,
1134 v. 20, p. 833–836, doi:10.1130/0091-7613(1992)020<0833:DFEFAL>2.3.CO;2.
- 1135 Sibson, R.H., 1985, A note on fault reactivation: *Journal of Structural Geology*, v. 7, p. 751–754,
1136 doi:10.1016/0191-8141(85)90150-6.
- 1137 Sibson, R.H., 1986, Brecciation processes in fault zones: Inferences from earthquake rupturing:
1138 *Pure and Applied Geophysics*, v. 124, p. 159–175, doi:10.1007/BF00875724.
- 1139 Sibson, R.H., 1990, Conditions for fault-valve behavior, *in Knipe, R.J., and Rutter, E.H., eds.,*
1140 *Deformation Mechanisms, Rheology, and Tectonics*: Geological Society of London Special
1141 Publication 54, p. 15–28, doi:10.1144/GSL.SP.1990.054.01.02.
- 1142 Sibson, R.H., Robert, F., and Poulsen, K.H., 1988, High-angle reverse faults, fluid-pressure
1143 cycling, and mesothermal gold-quartz deposits: *Geology*, v. 16, p. 551–555,
1144 doi:10.1130/0091-7613(1988)016<0551:HARFFP>2.3.CO;2.
- 1145 Smith, S.A.F., Holdsworth, R.E., Collettini, C., and Imber, J., 2007, Using footwall structures to
1146 constrain the evolution of low-angle normal faults: *Journal of the Geological Society of*
1147 *London*, v. 164, p. 1187–1191, doi:10.1144/0016-76492007-009.
- 1148 Smith, S.A.F., Collettini, C., and Holdsworth, R.E., 2008, Recognizing the seismic cycle along
1149 ancient faults: CO₂-induced fluidization of breccias in the footwall of a sealing low-angle
1150 normal fault: *Journal of Structural Geology*, v. 30, p. 1034–1046,
1151 doi:10.1016/j.jsg.2008.04.010.

- 1152 Storti, F., 1995, Tectonics of the Punta Bianca promontory: Insights for the evolution of the
1153 Northern Apennines–Northern Tyrrhenian Sea basin: *Tectonics*, v. 14, p. 832–847,
1154 doi:10.1029/95TC01203.
- 1155 Storti, F., Billi, A., and Salvini, F., 2003, Particle size distributions in natural carbonate fault
1156 rocks: Insights for non-self-similar cataclasis: *Earth and Planetary Science Letters*, v. 206,
1157 p. 173–186, doi:10.1016/S0012-821X(02)01077-4.
- 1158 Storti, F., Rossetti, F., Läufer, A., and Salvini, F., 2006, Consistent kinematic architecture in the
1159 damage zones of intraplate strike-slip fault systems in North Victoria Land, Antarctica, and
1160 implications for fault zone evolution: *Journal of Structural Geology*, v. 28, p. 50–63,
1161 doi:10.1016/j.jsg.2005.09.004.
- 1162 Talman, S.J., Wiwchar, B., Gunter, W.D., and Scarge, C.M., 1990, Dissolution kinetics of calcite
1163 in the H₂O–CO₂ system along the steam saturation curve to 210 °C, *in* Spencer, R.J., and
1164 Chou, I.M., eds., *Fluid–Mineral Interactions: A Tribute to H.P. Eugster*: Geochemical
1165 Society Special Publication 2, p. 41–55.
- 1166 Tarasewicz, J.P.T., Woodcock, N.H., and Dickson, J.A.D., 2005, Carbonate dilation breccias:
1167 Examples from the damage zone to the Dent fault, northwest England: *Geological Society of
1168 America Bulletin*, v. 117, p. 736–745, doi:10.1130/B25568.1.
- 1169 Veizer, J., Ala, D., Azmy, K., Bruckschen, P., Buhl, D., Bruhn, F., Carden, F.A.F., Diener, A.,
1170 Ebner, S., Godderis, Y., Jasper, T., Korte, C., Pawellek, F., Podlaha, O.G., and Strauss, H.,
1171 1999, ⁸⁷Sr/⁸⁶Sr, δ¹³C and δ¹⁸O evolution of Phanerozoic seawater: *Chemical Geology*,
1172 v. 161, p. 59–88, doi:10.1016/S0009-2541(99)00081-9.

- 1173 Verhaert, G., Muchez, P., Sintubin, M., Similox-Tohon, D., Vandycke, S., Keppens, E., Hodge,
1174 E.J., and Richards, D.A., 2004, Origin of palaeofluids in a normal fault setting in the Aegean
1175 region: *Geofluids*, v. 4, p. 300–314, doi:10.1111/j.1468-8123.2004.00094.x.
- 1176 Verhaert, G., Muchez, P., Keppens, E., and Sintubin, M., 2009, Fluid impact and spatial and
1177 temporal evolution of normal faulting in limestones. A case study in the Burdur-Isparta
1178 region (SW Turkey): *Geologica Belgica*, v. 12, p. 59–73.
- 1179 Videtich, P.E., and Matthews, R.K., 1980, Origin of discontinuity surfaces in limestones:
1180 Isotopic and petrographic data, Pleistocene of Barbados, West Indies: *Journal of*
1181 *Sedimentary Research*, v. 50, no. 3, p. 971–980, doi:10.1306/212F7B3A-2B24-11D7-
1182 8648000102C1865D.
- 1183 Walkden, G.M., and Williams, D.O., 1991, The diagenesis of the late Dinantian Derbyshire–East
1184 Midland carbonate shelf, central England: *Sedimentology*, v. 38, p. 643–670,
1185 doi:10.1111/j.1365-3091.1991.tb01013.x.
- 1186 Wickham, S.M., and Taylor, H.P., 1987, Stable isotope constraints on the origin and depth of
1187 penetration of hydrothermal fluids associated with Hercynian regional metamorphism and
1188 crustal anatexis in the Pyrenees: *Contributions to Mineralogy and Petrology*, v. 95, p. 255–
1189 268, doi:10.1007/BF00371841.
- 1190 Woodcock, N.H., and Mort, K., 2008, Classification of fault breccias and related fault rocks:
1191 *Geological Magazine*, v. 145, p. 435–440, doi:10.1017/S0016756808004883.
- 1192 Woodcock, N.H., Dickson, J.A.D., and Tarasewicz, J.P.T., 2007, Transient permeability and
1193 reseal hardening in fault zones: Evidence from dilation breccia textures, *in Lonergan, L.,*
1194 *Jolly, J.H., Rawnsley, K., and Sanderson, D.J., Fractured Reservoirs*: Geological Society of
1195 London Special Publication 270, p. 43–53, doi:10.1144/GSL.SP.2007.270.01.03.

1196 Woodcock, N.H., Sayers, N.J., and Dickson, J.A.D., 2008, Fluid flow history from damage zone
1197 cements near the Dent and Rawthey faults, NW England: *Journal of the Geological Society*
1198 of London, v. 165, p. 829–837, doi:10.1144/0016-76492007-133.

1199 Yin, A., 1989, Origin of regional, rooted low-angle normal faults: A mechanical model and its
1200 tectonic implications: *Tectonics*, v. 8, p. 469–482, doi:10.1029/TC008i003p00469.

1201 Zattin, M., Picotti, V., and Zuffa, G.G., 2002, Fission-track reconstruction of the front of the
1202 Northern Apennine thrust wedge and overlying Ligurian unit: *American Journal of Science*,
1203 v. 302, p. 346–379, doi:10.2475/ajs.302.4.346.

1204 Zhang, R., Hu, S., Zhang, X., and Yu, W., 2007, Dissolution kinetics of dolomite in water at
1205 elevated temperatures: *Aquatic Geochemistry*, v. 13, p. 309–338, doi:10.1007/s10498-007-
1206 9022-z.

1207 **FIGURE CAPTIONS**

1208 Figure 1. (A) Regional-scale geologic section of the Northern Apennines (after Molli, 2008; see
1209 inset for location; NA—Northern Apennines; SA—Southern Apennines). (B) Tectonic map of
1210 the Punta Bianca promontory and the surrounding region (same colors as A; PD—Pitelli
1211 detachment extensional fault system; TD—Tellaro detachment extensional fault system). (C)
1212 Geological cross section through the Punta Bianca promontory (modified from Federici and
1213 Raggi, 1975; *Carta Geologica d'Italia*, 2005). See part D for color scheme legend; s.l.—**sea level**.
1214 (D) Stratigraphic column of the Tuscan succession in the study area (after *Carta Geologica*
1215 *d'Italia*, 2005). Sst—sandstone; Sh—shales; Ls—limestone; Cht—chert; Mrlst—marls; Dol—
1216 dolostone; brec—breccia; MAC—Macigno Formation; STO—Scaglia Toscana Formation;
1217 MAI—Maiolica Formation; DSD—Diaspri Formation; POD—Marne a Posidonia Formation;
1218 LIM—Calccare Selcifero di Limano Formation; RSA—Rosso Ammonitico Formation; RER—

1219 Ferriera Formation; FBS—Biassa Formation; DMC—Dolomie del Monte Castellana Formation;
1220 PRT—Portoro Formation; LSP—La Spezia Formation; DCR—Dolomie di Coregna Formation;
1221 BML—Brecce di Maralunga Formation. Color scheme as in C; thick black lines with square
1222 symbols indicate the preferential location of major low-angle fault segments of the Tellaro
1223 detachment fault system. **[[Figure edits: Add lat and long to B? Fix spelling of Upper**
1224 **Jurassic in D.]]**

1225 Figure 2. Structural map of the Tellaro detachment (see Fig. 1B for location). (A) Geological
1226 map with the trace of the low-angle fault envelope, lower-hemisphere projections of structural
1227 data in the different sectors, and inferred tectonic transport directions indicated by white arrows
1228 (base map after Carta Geologica d'Italia, 2005); c.i.—**confidence interval**. (B) Cumulative
1229 structural data for the whole exposed area of the Tellaro detachment. **See Figure 1 caption for**
1230 **formation abbreviations. [[Figure edits: Add lat and long to map?]]**

1231 Figure 3. Outcrop-scale characteristics of the Tellaro detachment. (A) Punta delle Stelle,
1232 panoramic view from SE. (B) Interpretative line drawing of A (see Fig. 1 caption for formation
1233 abbreviations; s.l.—**sea level**). (C) Geologic cross section and structural data. (D) Detail of the
1234 **Rosso Ammonitico Formation (RSA)–Biassa Formation (FBS) contact** (see C for location). (E)
1235 Outcrop picture of the detachment (smooth surface highlighted by thick black line) with a meter-
1236 scale corrugation (black arrow) parallel to the tectonic transport direction (see Fig. 4 for detailed
1237 location). (F) Meter-scale folds associated with major corrugations of the detachment (see Fig. 4
1238 for detailed location). **[[Figure edits: Scale for D?]]**

1239 Figure 4. Photograph and interpretative line drawing of the Tellaro detachment at Punta delle
1240 Stelle, view from NW (see Fig. 2 for location; s.l.—**sea level**). A dolomitic breccia body is
1241 associated with the low-angle shear zone and crosscut by subsidiary high-angle faults. The near-

1242 horizontal surface in the foreground is affected by intense pressure solution S-C arrays (see Fig.
1243 1 caption for formation abbreviations). This outcrop has been affected by a rock fall, which
1244 partly covers the lowermost low-angle slip surface; for a pre-rock fall photo, see Figure 9c in
1245 Storti (1995).

1246 Figure 5. Detailed structural map of the Punta di Treggiano segment of the Tellaro detachment
1247 (see Fig. 2 for location; s.l.—**sea level**), and corresponding geologic cross section. Structural data
1248 collected in this sector are provided (c.i.—**confidence interval**). **See Figure 1 caption for**
1249 **formation abbreviations. [[Figure edits: Add lat and long to map? Fix spelling of**
1250 **Stereographic (top right).]]**

1251 Figure 6. Examples of deformation structures associated with the Tellaro detachment. (A) Small-
1252 scale shear planes and pressure solution seams organized in S-C arrays. (B) Major low-angle
1253 fault surface with centimeter-scale corrugations (big white arrow); tectonic transport direction is
1254 nearly orthogonal to the photo. Small white arrows indicate a synthetic shear. Pressure solution
1255 planes are indicated by wiggled black line, and differently oriented calcite vein trends are
1256 provided by double-sided black arrows. Photomicrograph of mutually crosscutting veins and
1257 pressure solution planes in inset. (C) Calcite veins organized in three systems (arrows) at outcrop
1258 scale, and photomicrograph shown in inset. (D) Calcite-filled fracture mesh in the footwall of a
1259 low-angle fault, close to the main slip surface. Individual fractures have short and curved
1260 geometries and are characterized by random orientations and crosscutting relationships.

1261 Figure 7. Photomicrograph (PM) of fault-related veins under plane light (PL), crossed polars
1262 (CP), and cathodoluminescence (CL) view. (A) Dolomitic host rock affected by successive
1263 veining (upper PM—PL, lower PM—CP). In chronological order, it is possible to recognize:
1264 fibrous dolomite vein, equigranular dolomite vein, dolomite microveins, and thin calcite

1265 reopenings at the margins of dolomite veins. (B) Protobreccia texture adjacent to dolomite vein
1266 (CP; see text for details). (C) Detail of A (PL). (D) Same as C (CL). (E) Type 1 calcite veins
1267 with equant to inequant granular textures (upper PM—PL, lower PM—CP). (F) Thick type 1
1268 calcite vein characterized by equant granular texture at the margins and parallel comb texture in
1269 the middle (upper PM—PL, lower PM—CP). (G) Thick type 1 calcite vein with multiple
1270 reopenings, crosscut by younger type 1 thin veins and type 2 calcite vein (PL; see text for
1271 details). (H) Same as G (CL). (I) Multiple generations of type 1 calcite veins (upper PM—PL,
1272 lower PM—CL). (J) Type 1 calcite vein (left PM—PL, right PM—CL). **[[Figure edits: Fix**
1273 **spelling of reopening.]]**

1274 Figure 8. Dolomitic breccias: photographs (P) and photomicrograph under plane light (PL),
1275 crossed polars (CP), and cathodoluminescence (CL) view. (A) Stained rock slab (P). Dolomitic
1276 clast (light gray) cemented by dolomite (dark gray) with fitted-fabric to mosaic texture.
1277 Dolomitic breccia is affected by partial rebrecciation cemented by ferroan calcite (black). Calcite
1278 veins (v) and pressure solution seams (arrows) sporadically affect the breccia, as shown in the
1279 inset. (B) Dolomitic clast (light gray) with mosaic to chaotic texture, cemented by dolomite (dark
1280 gray), without any fine-grained matrix (PL). (C) Detail of a dolomitic clast (PL). (D) Same as C
1281 (CP). (E) Calcite vein crosscutting the dolomitic breccia (PL). (F) Same as E (CL). (G)
1282 Centimeter-scale cataclastic band associated with the main slip surface at the base of a meter-
1283 scale breccia body (PL). Clasts become smaller and more rounded approaching the slip surface at
1284 the base of the photo. The original dilation breccia texture is visible at the top of the photo.
1285 White dashed line highlights the boundary between cataclastic band and dilational breccia.
1286 Figure 9. Stable isotope data, with different symbols used for host rocks, breccias, and veins
1287 (original data available in supplementary material **[see text footnote 1]**). (A) Samples from the

1288 whole Punta Bianca promontory (**SZ—shear zone**), with colors indicative of the different
1289 structural positions. Reference values of the same host rocks from different areas: (1) Cortecchi et
1290 al. (1992)[[**The in-text citation "Cortecchi et al. (1992)" is not in the reference list.**]]; (2)
1291 Gasparrini et al. (2013)[[**The in-text citation "Gasparrini et al. (2013)" is not in the**
1292 **reference list.**]]. (B) Tellaro detachment samples, with colors indicative of sample composition
1293 (calcite or dolomite). (C) Tellaro detachment calcite vein samples, with colors indicative of type
1294 1 and type 2 generations. Stratigraphic formations: FBS—Biassia Formation; DMC—Dolomie
1295 del Monte Castellana Formation; LSP—La Spezia Formation; **VSMOW—Vienna standard mean**
1296 **ocean water; VPDB—Vienna Peedee belemnite.**

1297 Figure 10. Fluid inclusions in carbonate veins. (A) Cloudy dolomite crystal with abundant
1298 inclusions and arrows indicating particularly large inclusions. (B) Clear dolomite crystal with
1299 few inclusions. Dashed lines indicate alignment of (pseudo)secondary inclusions; arrows indicate
1300 isolated inclusions. (C) Type 1 calcite crystal with secondary inclusions aligned along the
1301 twinning planes and isolated inclusions in the space in-between. (D) Details of C. Dashed lines—
1302 inclusions aligned along twinning planes; arrows—isolated inclusions. (E–F) Type 2 calcite
1303 crystals with monophasic fluid inclusions (arrows). (G) Histogram showing the distribution of
1304 homogenization temperatures (T_h) in dolomite (PB04–1, PB05–1) and type 1 calcite veins
1305 (PB21–2, PB22–3, PB22–2, PB17–1), bin width 10 °C, color-coded according to the veins in
1306 which inclusions were measured. (H) Scatterplot of homogenization (T_h) versus final ice melting
1307 ($T_{m\ ice}$) temperatures, using same samples and color code as G. (I) Histogram showing the
1308 distribution of final ice melting temperatures ($T_{m\ ice}$) in type 2 calcite veins, with bin width 0.5
1309 °C. Original data used for plots G–I are available as supplementary material (**see text footnote 1**).

1310 Figure 11. Type 1 calcite veins: radiogenic strontium (one analysis per vein) and stable oxygen
1311 (several analyses per vein) isotope compositions (original data available as supplementary
1312 material [see text footnote 1]). Gray boxes indicate the expected values for Tuscan succession
1313 carbonates and Upper Miocene (UM) seawater (reference values from McArthur et al., 2001;
1314 Veizer et al., 1999). **VSMOW—Vienna standard mean ocean water; VPDB—Vienna Peedee**
1315 **belemnite.**

1316 Figure 12. (A) Pressure correction to estimate the trapping conditions for calcite and dolomite
1317 veins. Specific isochores were built based on the measured T_h and $T_{m\ ice}$ data. A geothermal
1318 gradient of 20 °C/km was used as an independent constraint to build two pressure-temperature
1319 gradients assuming hydrostatic and lithostatic fluid pressure, respectively. The two dolomite
1320 veins show similar results and are represented by a single isochore; specific isochores were built
1321 for each type 1 calcite vein; type 2 calcite veins are plotted together in the light-gray area since
1322 their trapping temperature is only constrained as <70 °C. (B) Oxygen isotope fractionation
1323 during equilibrium precipitation: calcite (vertical axis) and fluid (curves) composition as a
1324 function of temperature. Black and white symbols indicate the different type 1 and type 2 calcite
1325 veins (see text for details). **VSMOW—Vienna standard mean ocean water.** (C) Schematic
1326 diagram summarizing the timing and depth conditions of the different carbonate precipitation
1327 stages (see text for details). Symbols indicate dolomite and type 1 calcite veins as in B and C.

1328 Figure 13. Average attitude of the major low-angle and subsidiary high-angle faults of the
1329 Tellaro detachment (TD) fault system. (A) Present-day attitude, possibly affected by
1330 postkinematic passive rotation due to superimposed faulting. (B) Maximum possible dip during
1331 main kinematic activity, obtained by restoration of subsidiary faults to symmetric conjugate

1332 pairs. Original synkinematic attitude of the fault system lies somewhere between the two
1333 represented end members (see text for details).

1334 Figure 14. (A) Pore fluid factor ($\lambda = P_f/\sigma_v$) vs. differential stress ($\delta\sigma = \sigma_1 - \sigma_3$) diagram showing
1335 the failure envelope for carbonate rocks at 4 km depth, and the reshear envelope of misoriented
1336 planes (see text for details). (B) Pore fluid factor vs. differential stress diagram showing failure
1337 envelopes for carbonate rocks and misoriented fault planes at different depths. (C) Transient
1338 permeability due to cyclical episodes of veining and vein cementation (light gray—carbonate
1339 host rock; white—open vein; black—vein infilling). (D) Transient permeability due to veining,
1340 cementation, and metasomatic host-rock dolomitization, brecciation, and breccia cementation
1341 (light gray—carbonate host rock; white—open vein; medium gray—dolomitized host rock; dark
1342 gray—dolomitic breccia cement; black—vein infilling). (E) Relationships between brittle
1343 fracturing and reseal healing and resultant fault zone permeability and pore fluid pressure, during
1344 the kinematic activity and progressive exhumation of the fault system. **Variables:** σ_n —normal
1345 stress; P_f —pore fluid pressure; τ —shear stress; T_0 —tensile strength; C_0 —cohesive strength; μ —
1346 coefficient of friction for intact rock; μ_s —coefficient of friction for preexisting cohesionless
1347 plane; θ_{opt} —angle between principal stress and optimally oriented shear plane; θ —angle between
1348 principal stress and misoriented shear plane; Z —depth; k —permeability; size—total dimension
1349 of the Tellaro detachment fault system. **[[Figure edit: In bottom graph of part E, change
1350 citations to Fig. 14A, 14B, 14C, 14D, and 14E to Fig. 15A, 15B, 15C, 15D, and 15E
1351 respectively.]]**

1352 Figure 15. Evolutionary model of the Tellaro detachment: schematic cartoon illustrating the
1353 proposed structural and paleofluid evolution of the Tellaro detachment into four deformation
1354 events (Lst—limestone; Dol—dolomite; letters A to E refer to Fig. 14E).

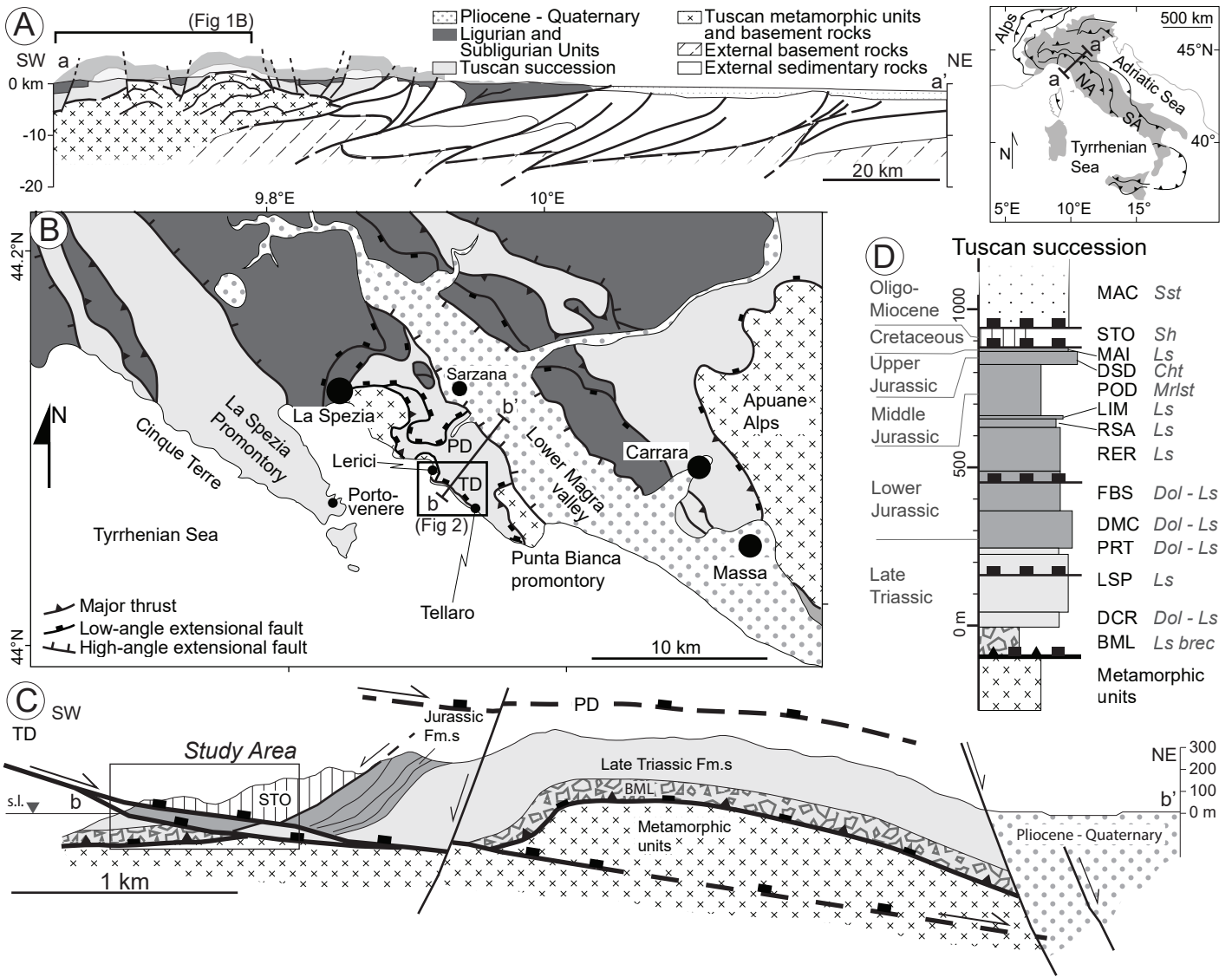


Fig 1 - Clemenzi et al

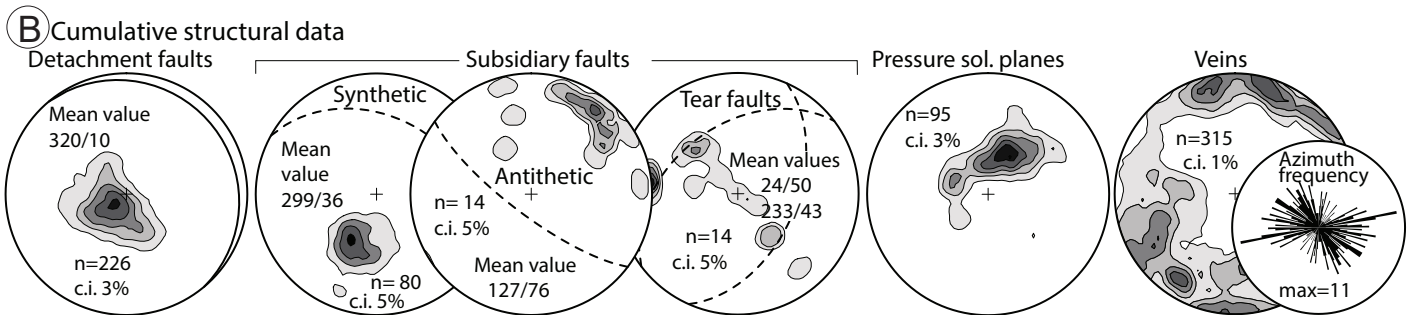
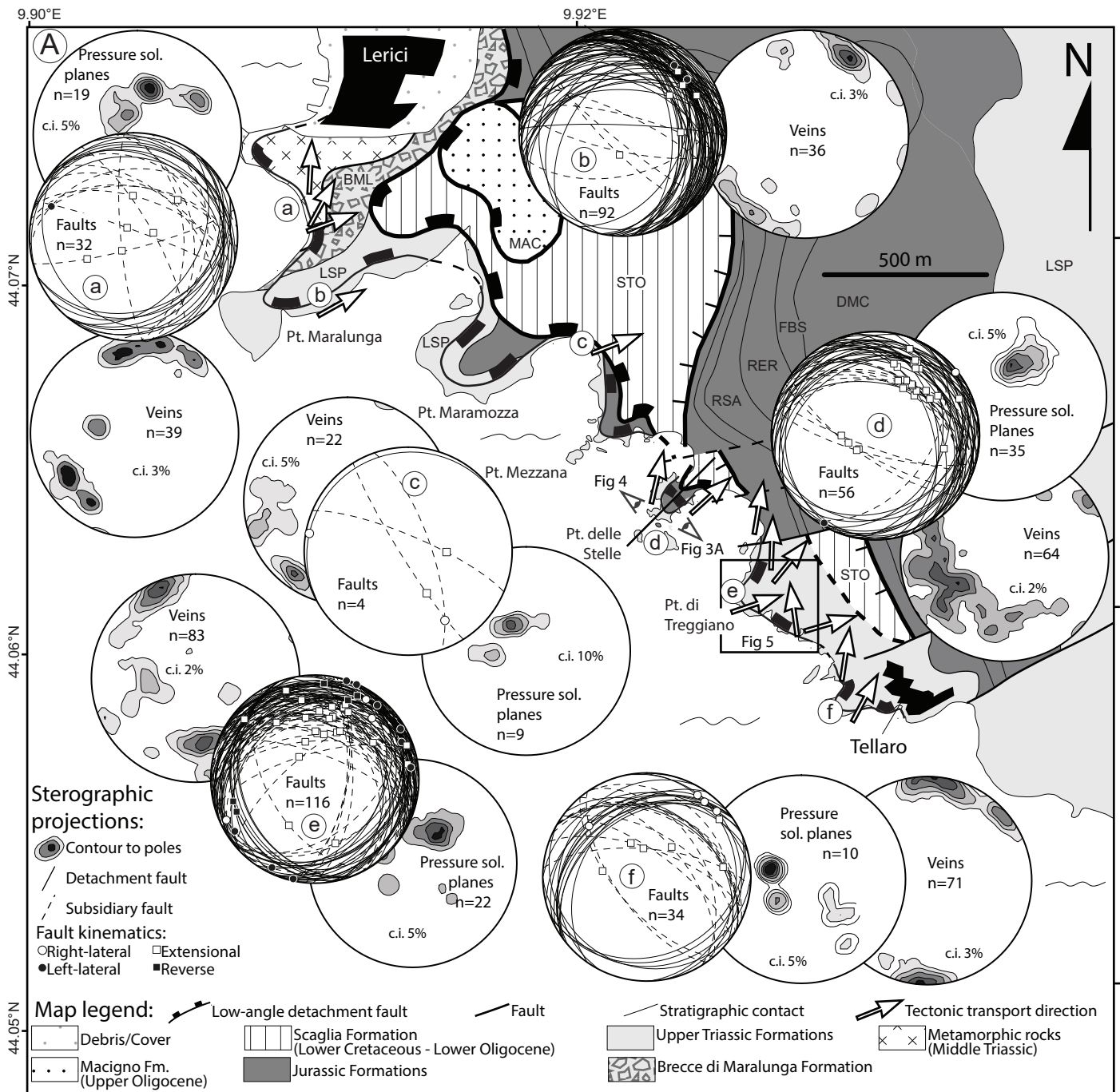


Fig 2 - Clemenzi et al

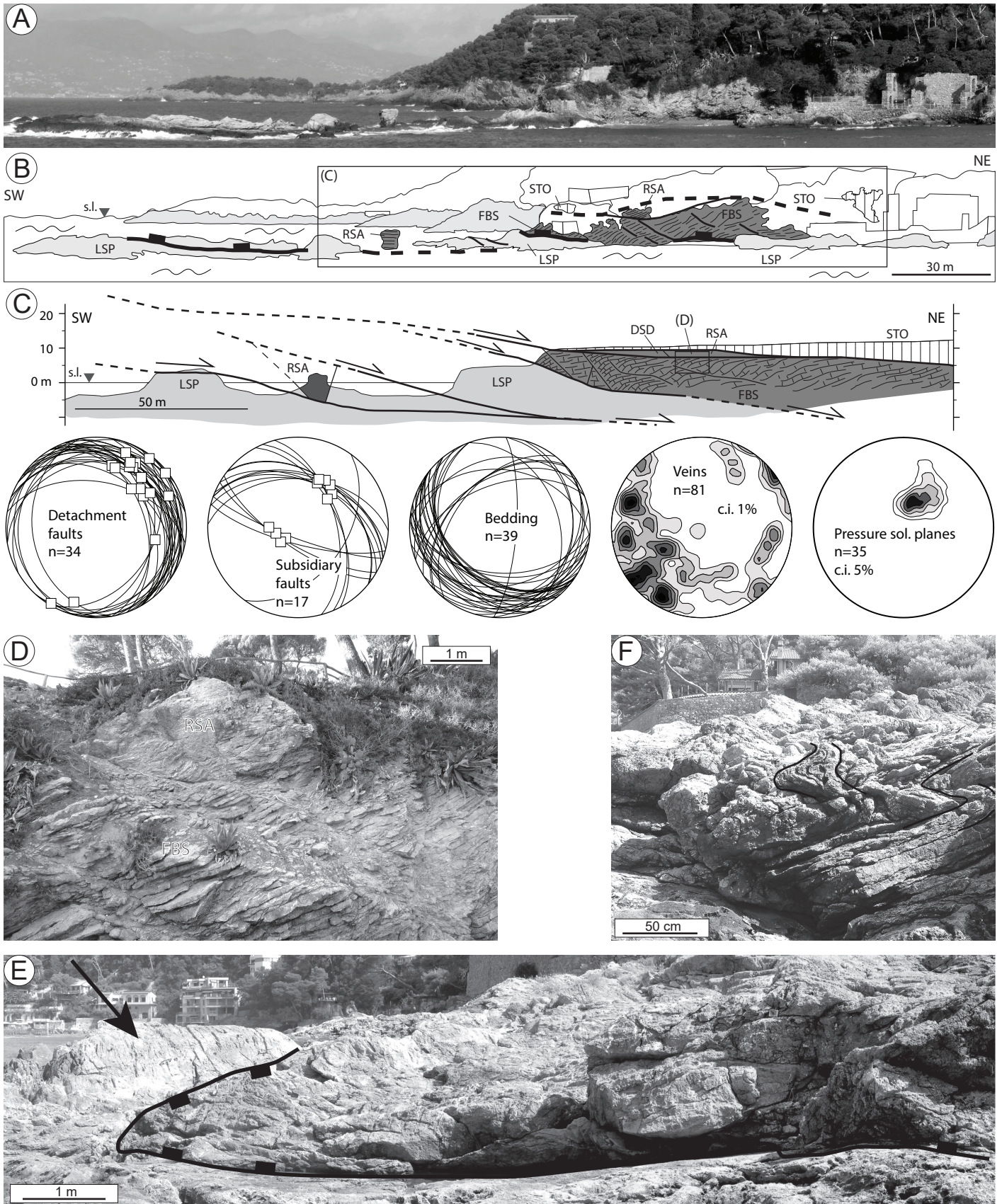


Fig 3 - Clemenzi et al

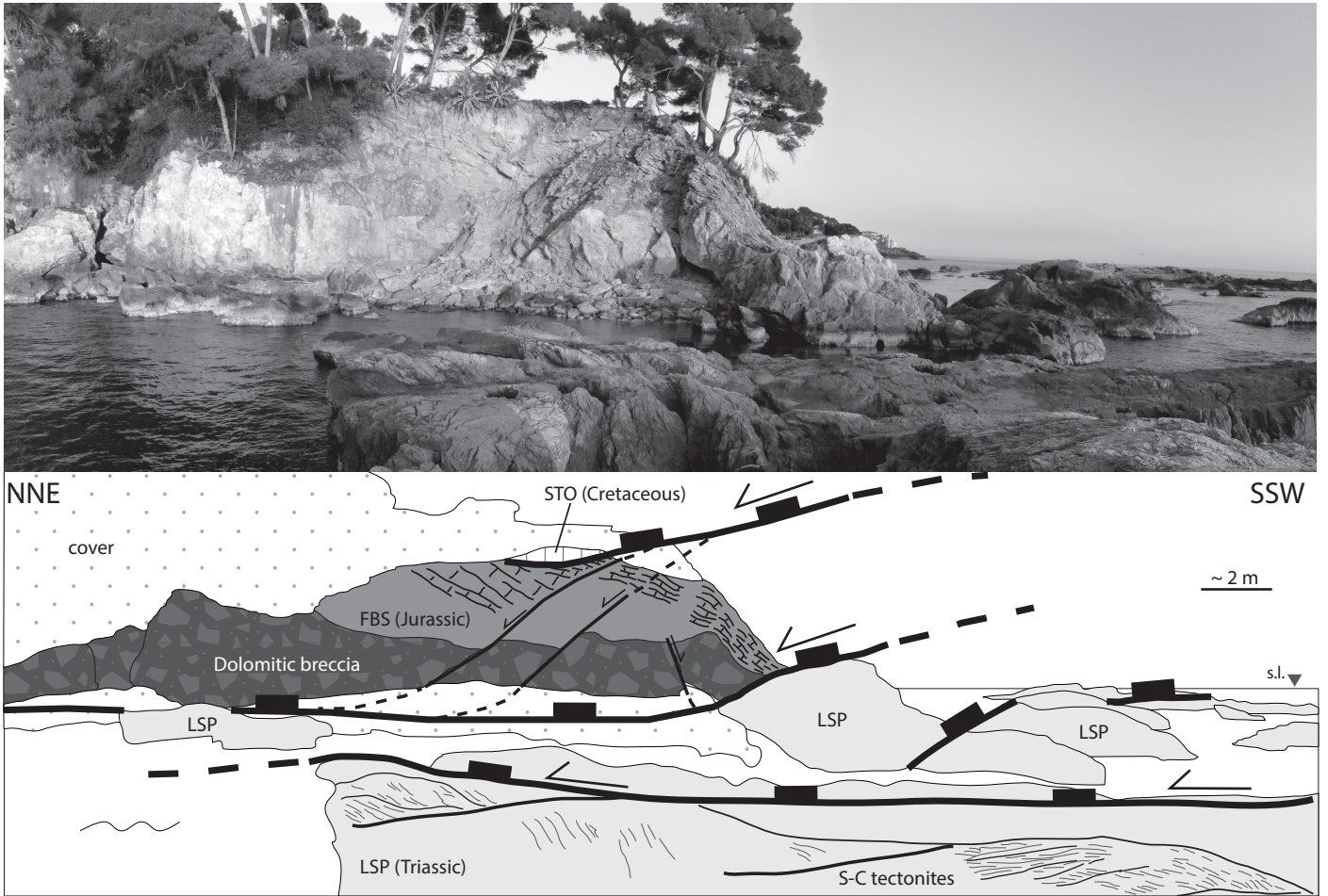


Fig 4 - Clemenzi et al

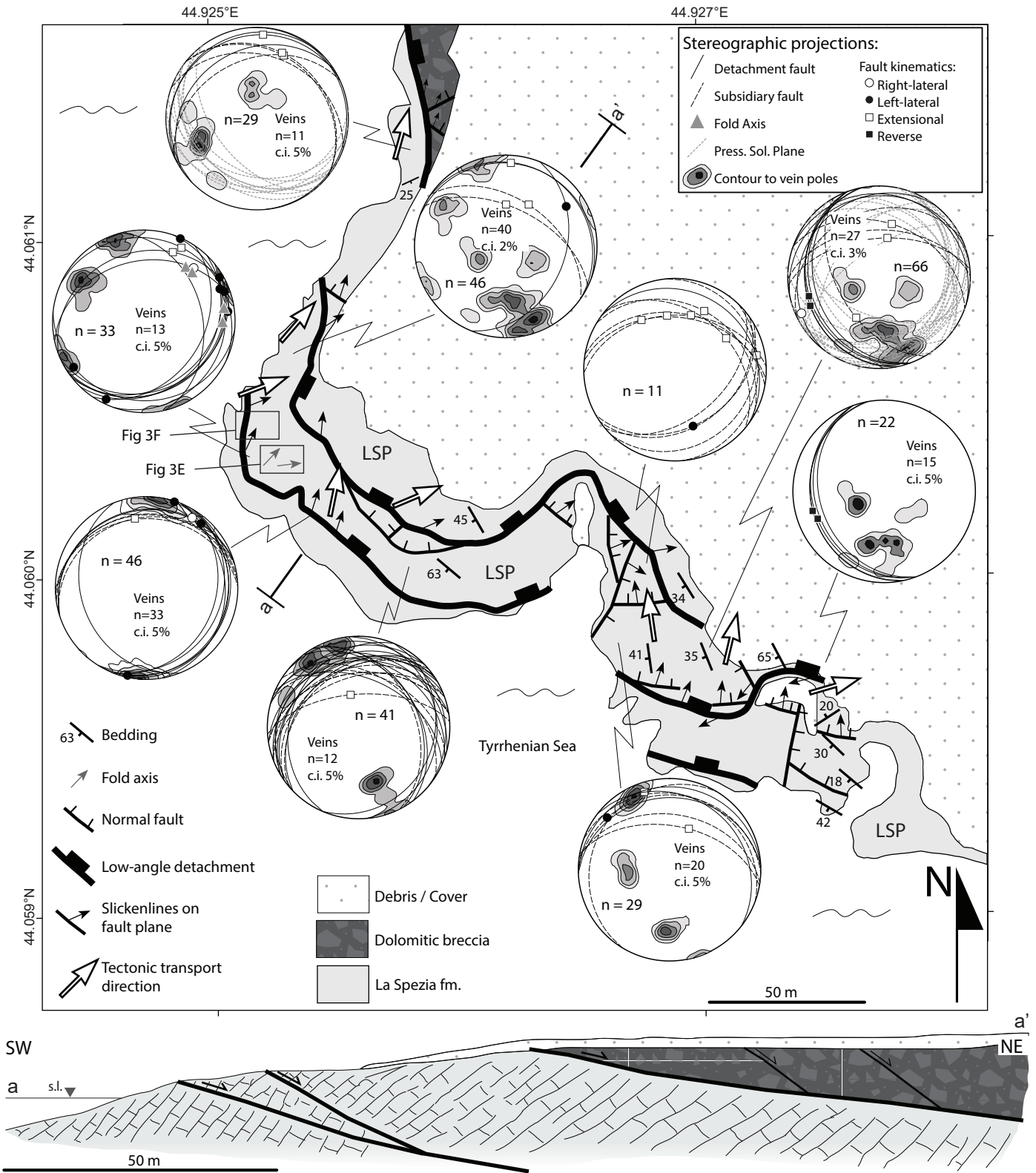


Fig 5 - Clemenzi et al

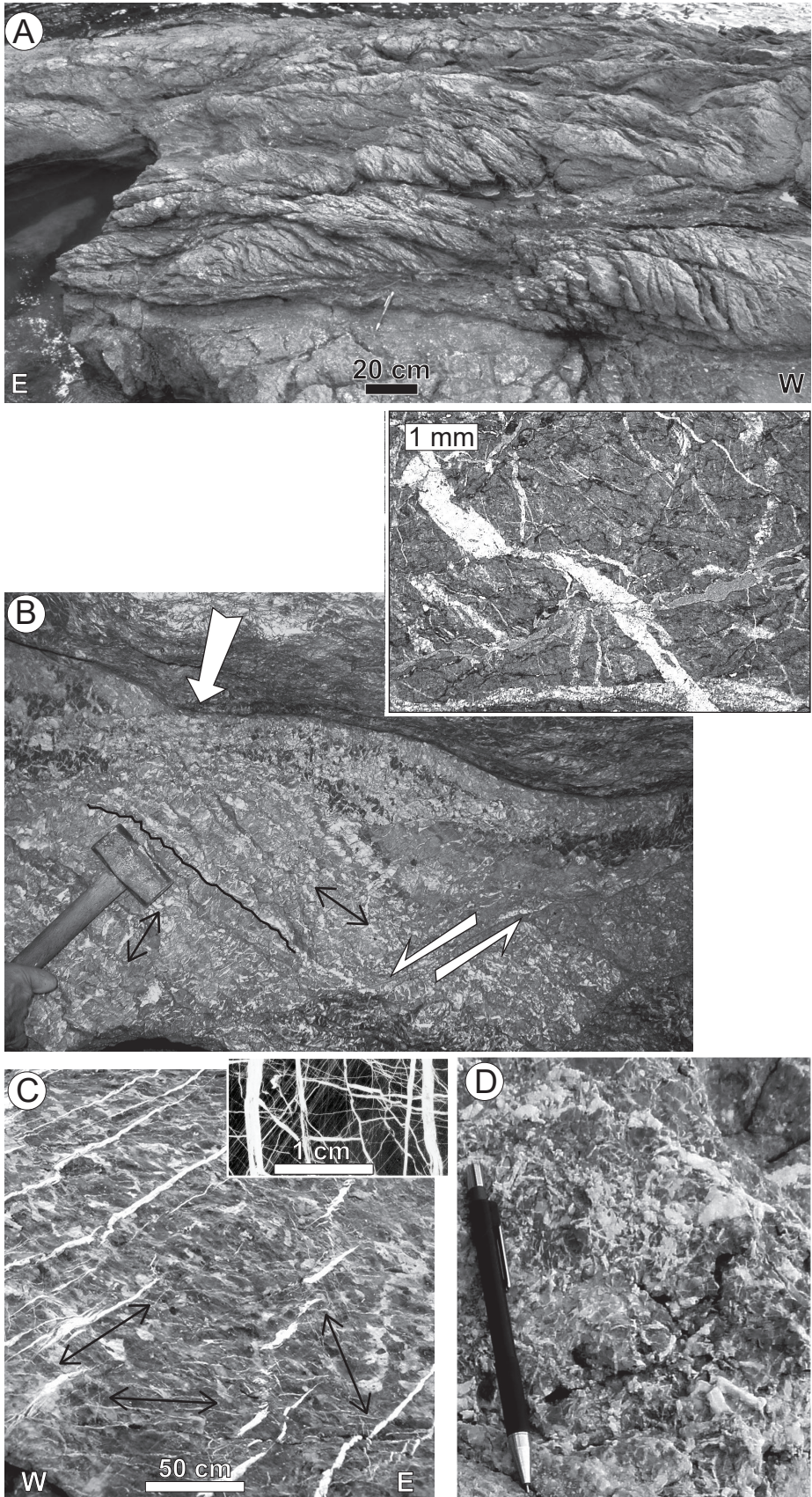


Fig 6 - Clemenzi et al

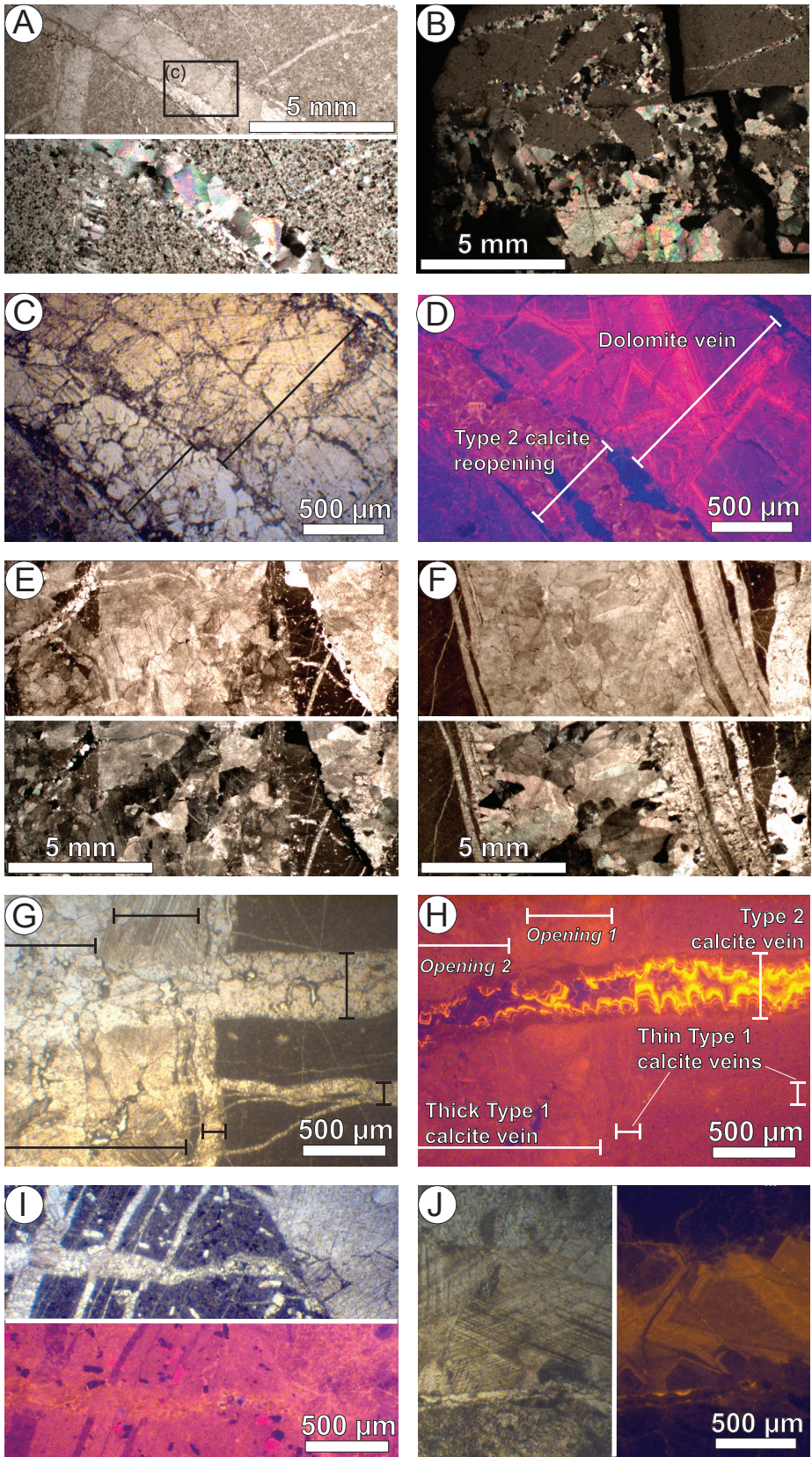


Fig 7 - Clemenzi et al

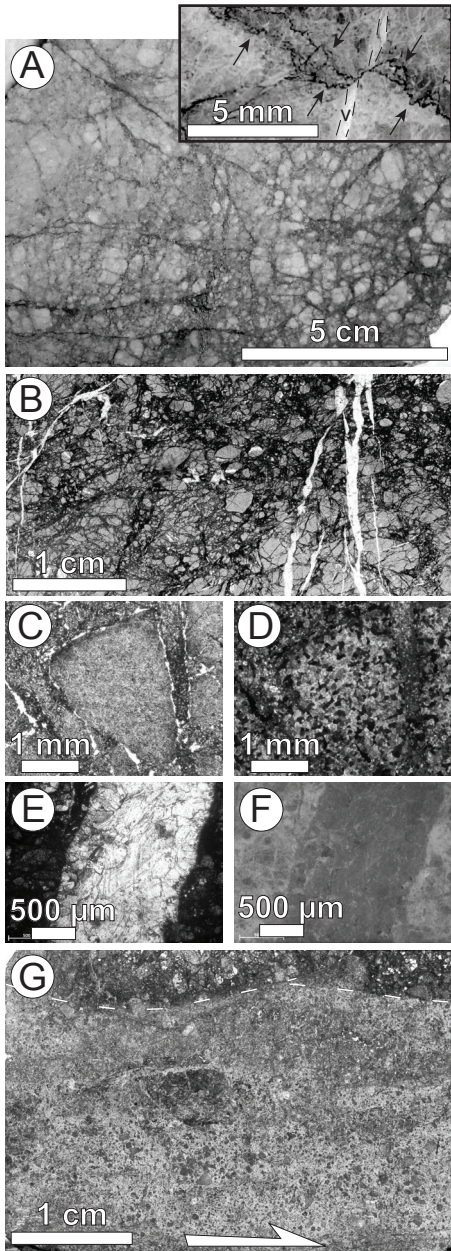


Fig 8 - Clemenzi et al

A All samples
 ▲ Breccia × Host ● Vein
 ■ Background def ■ Pitelli detach
 □ Punta Bianca SZ ■ Tellaro detach
 a b

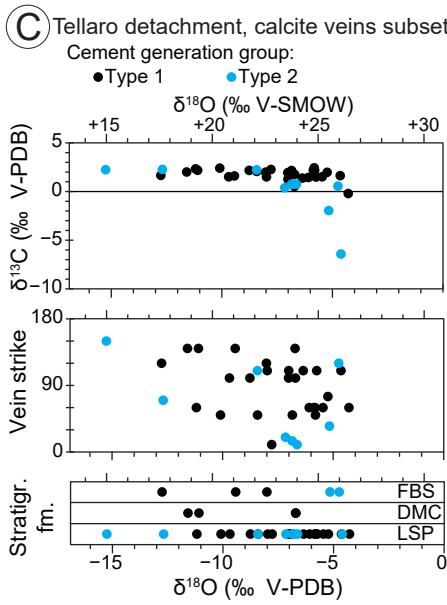
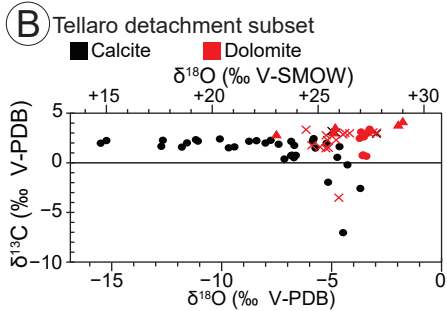
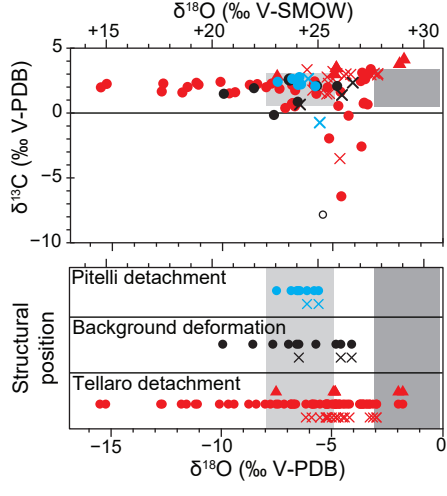


Fig 9 - Clemenzi et al

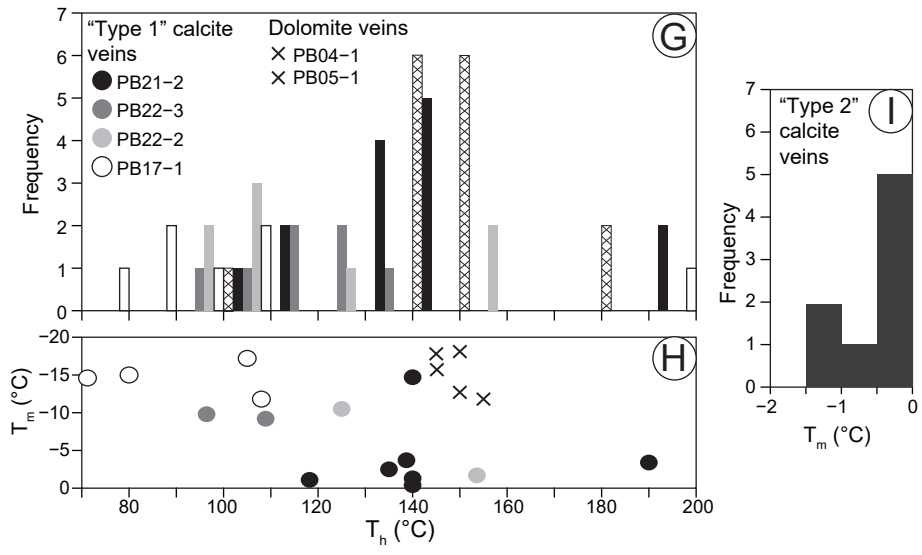
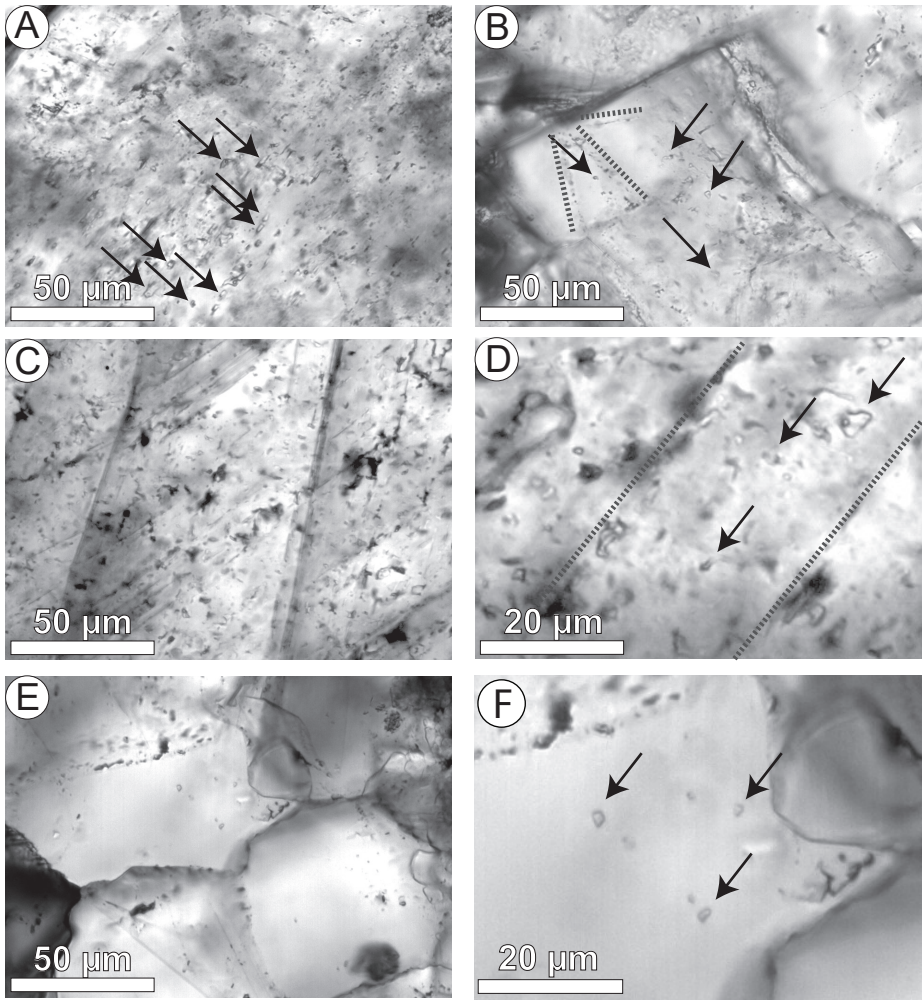
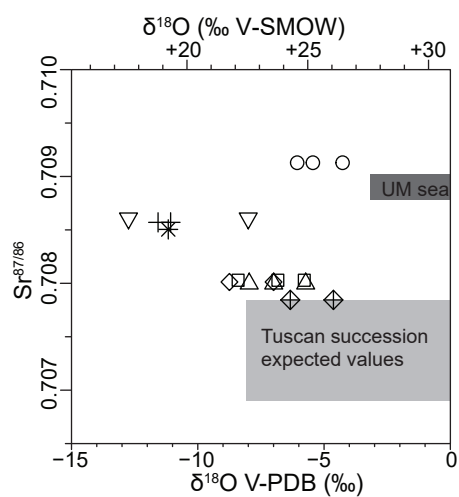


Fig 10 - Clemenzi et al



Samples (and available trapping temperature)

□ PB21-2 (190°C)	+ PB11-1
△ PB22-3 (150°C)	▽ PB07-1
□ PB22-2 (120°C)	* PB21-3
○ PB17-1 (95°C)	◇ PB22-1

Fig 11 - Clemenzi et al

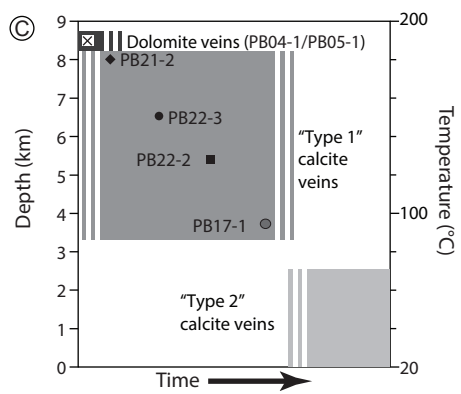
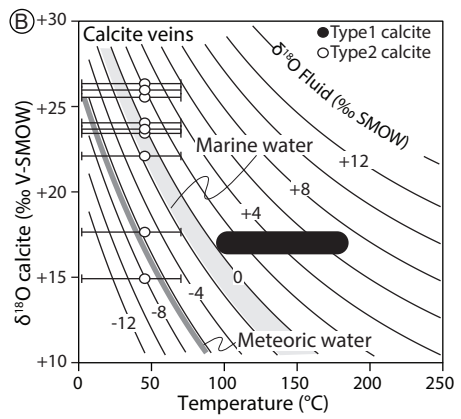
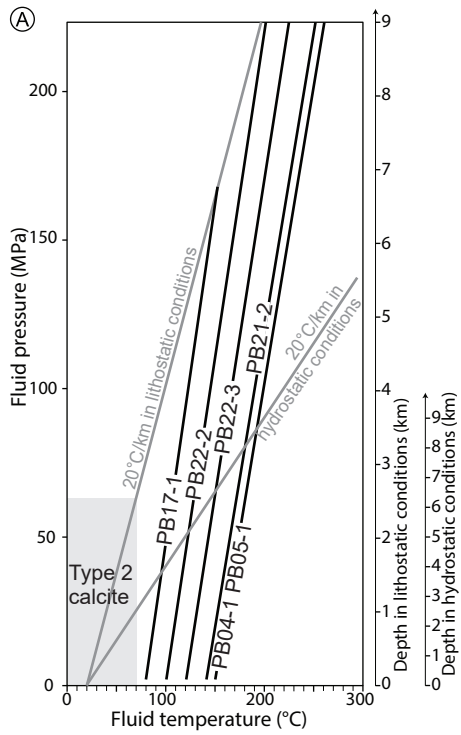


Fig 12 - Clemenzi et al

Average attitude of TD structures

Low-angle detachment faults
Subsidiary faults

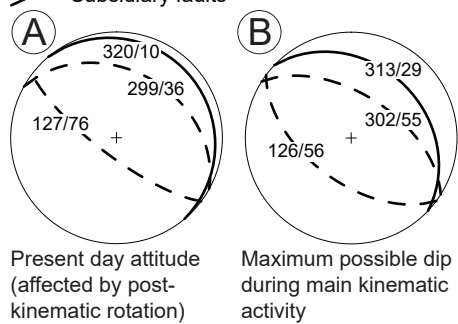


Fig 13 - Clemenzi et al

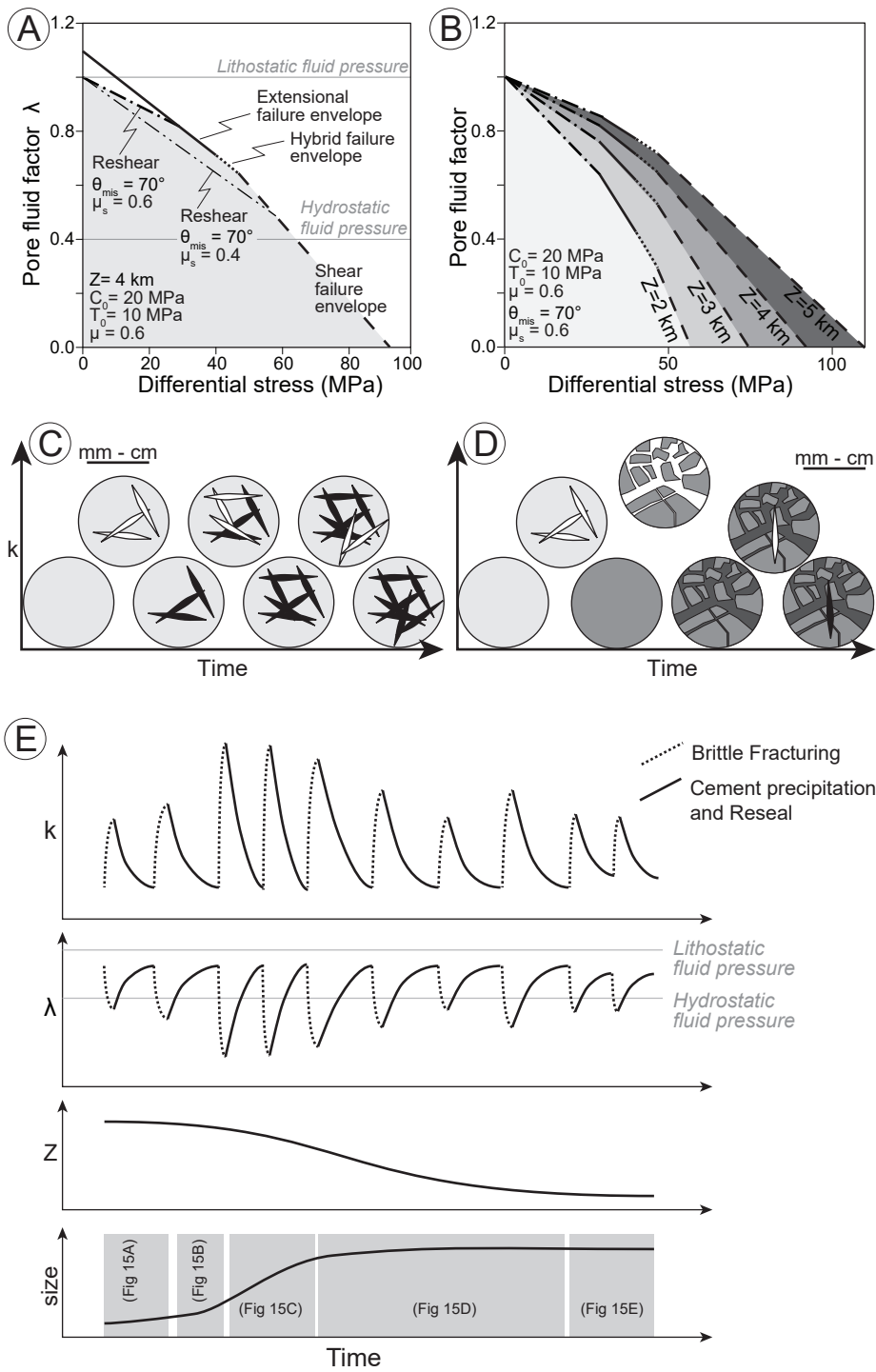


Fig 14 - Clemenzi et al

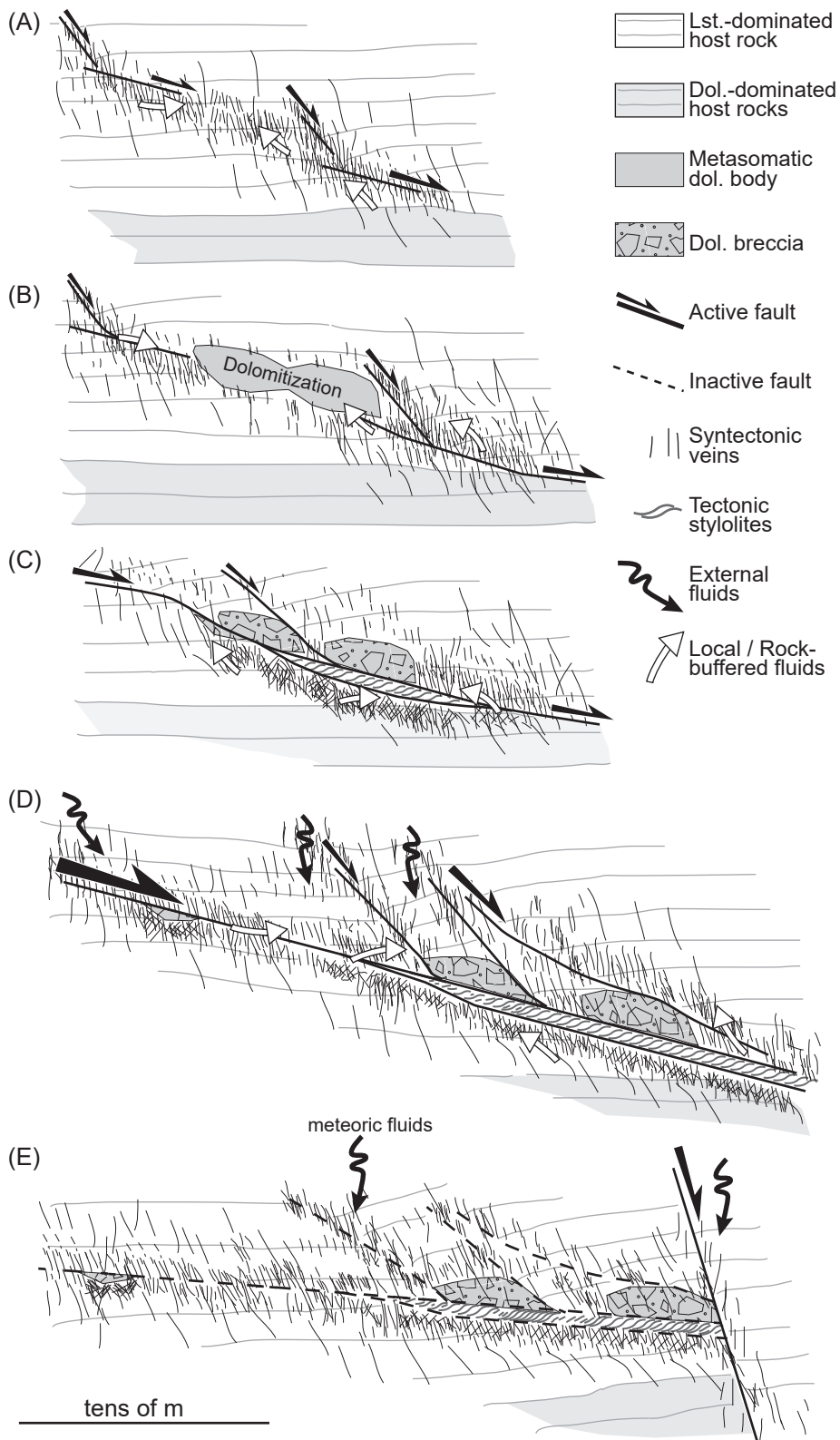


Fig 15 - Clemenzi et al